Drop Size Distributions and Radar Observations of Convective and Stratiform Rain over the Equatorial Indian and West Pacific Oceans

ELIZABETH J. THOMPSON, STEVEN A. RUTLEDGE, AND BRENDA DOLAN

Department of Atmospheric Science, Colorado State University, Fort Collins, Colorado

MERHALA THURAI

Department of Electrical and Computer Engineering, Colorado State University, Fort Collins, Colorado

(Manuscript received 17 July 2014, in final form 25 June 2015)

ABSTRACT

Two-dimensional video disdrometer (2DVD) data were analyzed from two equatorial Indian (Gan) and west Pacific Ocean (Manus) islands where precipitation is primarily organized by the intertropical convergence zone and the Madden–Julian oscillation (MJO). The 18 (3.5) months of 2DVD data from Manus (Gan) Island show that 1) the two sites have similar drop size distribution (DSD) spectra of liquid water content, median diameter, rain rate R, radar reflectivity z, normalized gamma number concentration N_w, and other integral rain parameters; 2) there is a robust N_w-based separation between convective (C) and stratiform (S) DSDs at both sites that produces consistent separation in other parameter spaces.

The 2DVD data indicate an equatorial, maritime average C/S rainfall accumulation fraction (frequency) of 81/19 (41/59) at these locations. It is hypothesized that convective fraction and frequency estimates are slightly higher than previous radar-based studies, because the ubiquitous weak, shallow convection ($<10\,\mathrm{mm\,h^{-1}}$) characteristic of the tropical warm pool is properly resolved by this high-resolution DSD dataset and identification method. This type of convection accounted for about 30% of all rain events and 15% of total rain volume. These rain statistics were reproduced when newly derived C/S $R(z)$ equations were applied to 2DVD-simulated reflectivity. However, the benefits of using separate C/S $R(z)$ equations are only realizable when C/S partitioning properly classifies each rain type. A single $R(z)$ relationship fit to all 2DVD data yielded accurate total rainfall amounts but overestimated (underestimated) the stratiform (convective) rain fraction by ±10% and overestimated (underestimated) stratiform (convective) rain accumulation by +50% (−15%).

1. Background and motivation

The majority of the world's rainfall occurs in the tropics, particularly over the warm pool spanning the equatorial Indian and west Pacific Oceans. Attributing rainfall to certain cloud types (i.e., shallow, congestus, or deep convection, stratiform rain, or a mixture thereof) is of critical importance for diagnosing the resulting vertical distribution of latent heating (Johnson et al. 1999; Schumacher et al. 2004), which can drive convergence and vertical motion (Matsuno 1966; Yanai et al. 1973; Zhang and Hagos 2009). Toward this end, identifying dominant modes of tropical, oceanic rain variability is important because this is still a major source of uncertainty in ground-based, shipborne, and spaceborne radar rainfall estimation (Munchak et al. 2012). For example, many studies have thoroughly detailed why and how cloud microphysical processes and vertical motions differ during convective (C) and stratiform (S) rain, which lead to characteristically different drop size distributions (DSDs) in each rain type (Williams et al. 1995; Tokay and Short 1996; Houze 1997; Tokay et al. 1999; Atlas et al. 1999, 2000; Bringi et al. 2003, hereafter BR03; Houze 2004; Bringi et al. 2009, hereafter BR09; Thurai et al. 2010, hereafter TH10; Schumacher et al. 2015; Zhu et al. 2015). There is also a region where (or time period when) active convective updrafts might be decaying into stratiform precipitation (Biggerstaff and Houze 1993; Braun and Houze 1994; Williams et al. 1995; Uijlenhoet et al. 2003; Sharma et al. 2009). These resulting DSDs lie between convective and stratiform. Additionally, marked differences exist between continental and maritime DSDs, both

Corresponding author address: Elizabeth J. Thompson, Department of Atmospheric Science, Colorado State University, 1371 Campus Delivery, Fort Collins, CO 80523-1371.
E-mail: liz@atmos.colostate.edu

DOI: 10.1175/JAS-D-14-0206.1

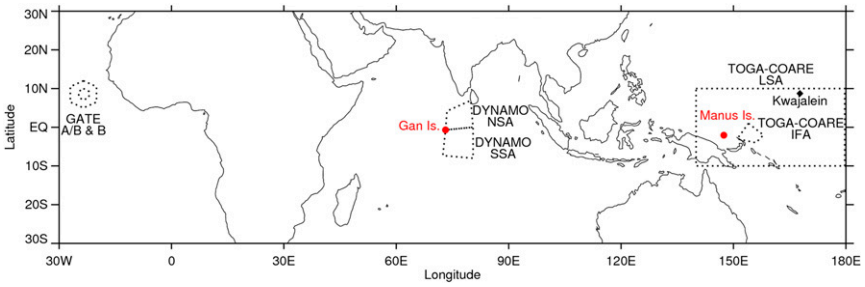

FIG. 1. DYNAMO northern (NSA) and southern sounding arrays (SSA), TOGA COARE intensive flux (IFA) and large sounding arrays (LSA), and GATE domains. The MISMO domain is a triangle in the same place as the DYNAMO NSA, but without the northwest island. Gan Island is within the DYNAMO and MISMO domains, while Manus Island and Kwajalein (diamond) were included in the TOGA COARE array.

of which produce convective and stratiform rain of varying intensities, efficiencies, and integral rain parameters, based on differences in updraft intensity and subcloud processes (Twomey 1977; Ulbrich and Atlas 1978; Zipser and LeMone 1980; Zipser 2003; Ulbrich and Atlas 2007; Minor et al. 2011; Wilson et al. 2013; Kumjian and Prat 2014).

The primary goal of this study is to investigate DSDs of equatorial, oceanic rainfall, which are less often studied because of their remote location, despite their contribution to the global hydrologic cycle. To do so, we take advantage of two long-term 2D video disdrometer (2DVD) datasets over the equatorial Indian and west Pacific Oceans, at Gan (3.5-month record) and Manus (18-month record) Islands, respectively (Fig. 1). BR03 identified maritime and continental convective DSD "clusters," as well as a linear variation of stratiform rain in the normalized gamma number concentration and median volume diameter $[N_w(D_0)]$ plane, which can be measured by disdrometers or derived from dual-polarization radar data. Their work involved DSD quantities from selected rain events in Florida, coastal Australia, Austria, Puerto Rico, Brazil, Kwajalein, Colorado, Papua New Guinea, and the South China Sea, as well as a mean of many west Pacific warm pool events. A separation line between convective and stratiform rain was determined by BR09 using the Darwin, Australia, datasets. DSDs were considered convective (stratiform) if N_w was greater (less) than a naturally emerging separator line: $\log_{10}$-$N_w^{\mathrm{SEP}} = -1.6D_0 + 6.3$. This partitioning method was found to be consistent with data from selected rain events in BR03 and with more data from Darwin by TH10 and Penide et al. (2013). TH10 also found agreement between the DSD-based $N_w(D_0)$ C/S partitioning method and the widely used Steiner et al. (1995) radar reflectivity-based partitioning algorithm using data from Darwin. This radar method identifies convective cores based on a reflectivity threshold and whether localized regions of reflectivity stand out relative to the smoothed, background reflectivity field, which can be modified for particular regions and radar data resolutions (Yuter and Houze 1997, 1998).

The classification and rain attribution of shallow, weak cumulus convection are critical, because this cloud type is ubiquitous across the warm pool (Johnson et al. 1999; Rauber et al. 2007; Jakob and Schumacher 2008; Barnes and Houze 2013), where the atmosphere is conditionally unstable below the equivalent potential temperature θ_e minimum (Lilly 1960). However, this relatively shallow and weak oceanic convection is not dominant in coastal or continental boundary layers, which likely explains its underrepresentation in BR03, BR09, and TH10, which consist of data mostly from midlatitude and subtropical land locations near oceans. Shallow, maritime, tropical convective clouds moisten the lower troposphere (Nitta and Esbensen 1974; Lin and Johnson 1996; Johnson and Lin 1997; Johnson et al. 1999) and may play an important role in Madden–Julian oscillation (MJO) evolution (Kemball-Cook and Weare 2001; Kiladis et al. 2005; Benedict and Randall 2007; Seo et al. 2014; Ruppert and Johnson 2015; Barnes et al. 2015). However, they are difficult to detect and track because of limited vertical, horizontal, and temporal resolution and the minimum detectable signals of many remote sensing platforms (Schumacher and Houze 2003; Jakob and Schumacher 2008; Funk and Schumacher 2013; Ruppert and Johnson 2015). The "stretched building block" hypothesis by Mapes et al. (2006) explains how stratiform clouds and all three major convective cloud types (shallow, congestus, and deep) are usually present over relatively large areas of the tropics, but some become more dominant than others during certain phases of the MJO. This is also consistent with recent MJO observational studies in the equatorial Indian and west Pacific Oceans (Riley et al. 2011; Barnes and Houze 2013; Zuluaga and Houze 2013; Powell and Houze 2013; Rowe and Houze 2014; Xu and Rutledge 2014, 2015; Barnes et al. 2015).

Current DSD partitioning methods have not comprehensively considered tropical, oceanic convection. In fact,

close inspection of Okinawa warm, shallow, convection DSD from TH10, Darwin maritime convection data from BR03, Darwin premonsoon-season data from BR09, and Darwin wet-season data from Bringi and Chandrasekar (2001, hereafter BC01) reveals that weak, shallow, maritime convection does not uniformly lie on the convective side of the subtropical, continental BR09 separator line. In contrast to continental convection, these maritime convective storms are characteristic of warm rain processes [i.e., condensation and collision–coalescence at temperatures > 0°C (Pruppacher and Klett 1997; Cotton et al. 2011)]. These processes result in high N_w but relatively low D_0. The inclusion of continental convection (~hailstorms) in BR09 caused their separator line to be sloped downward toward low N_w and large D_0 (BR03). These more intense continental storms containing vigorous mixed-phase processes and much evaporation are common over tropical land but rare over tropical oceans (Kumjian and Prat 2014; Rowe and Houze 2014). Therefore, the remote oceanic, tropical DSD of interest in the current study might warrant a different C/S separation method than the subtropical, continental BR09 line. The current study's primary goal is to analyze the C/S DSD variability and radar characteristics of a long-term tropical, equatorial, maritime dataset not available in previous studies.

The secondary goal of this study is to utilize the DSD measurements to form single-polarization radar-based rainfall estimation equations for these oceanic, tropical rain regimes. Many power-law equations have been developed to relate radar reflectivity [Z_h (dBZ) or z (mm^6 m^{-3})] to rainfall rate R (mm h^{-1}) for characteristic modes of DSD variability in particular regions based on the cloud microphysical processes encountered there (Battan 1973; Ulbrich and Atlas 1978; Atlas et al. 1984; Ulbrich and Atlas 1998; Steiner et al. 2004; Ryzhkov et al. 2005). The current study intends to build upon many previous rainfall-estimation-focused studies that used shorter-time-record DSD data from various instruments in the equatorial Atlantic Ocean (Cunning and Sax 1977; Austin and Geotis 1979; Hudlow 1979), the west Pacific Ocean (Tokay and Short 1996; Yuter and Houze 1997; Atlas et al. 1999; Tokay et al. 1999; Atlas et al. 2000; Atlas and Ulbrich 2000; Ulbrich and Atlas 2002), and other coastal, subtropical locations (Keenan et al. 2001; BR03, BR09, Bringi et al. 2011, 2012; TH10). The equatorial Indian Ocean has been relatively less studied.

Following this introduction, Section 2 describes the measurement systems and data processing involved in this study. Section 3 compares distributions of DSD R, z, number concentration, drop diameters, and liquid water content from the two equatorial (Indian and west Pacific) sites, which are shown to be similar. Radar data are used in section 4 to investigate the storm characteristics associated with each mode of DSD variability observed at Gan Island. Section 5 elaborates on a physically based separation found between convective and stratiform precipitation using DSD number concentration. We also quantify the sensitivity of C/S rain statistics to this separation method. New $R(z)$ equations for all, convective, and stratiform rain are presented for the equatorial Indian and west Pacific Ocean sites. The potential sensitivity of rainfall statistics to different $R(z)$ equations is discussed in section 6. Conclusions are found in section 7.

2. Data and methods

a. Domain and radar data

Figure 1 shows Gan and Manus Islands, as well as other locations of tropical, oceanic DSD research, such as Kwajalein and the domains of the 1974 Global Atmospheric Research Program (GARP) Atmospheric Tropical Experiment (GATE; Hudlow 1979), the 1992–93 Tropical Ocean Global Atmosphere Coupled Atmosphere–Ocean Response Experiment (TOGA-COARE; Webster and Lukas 1992), and the Mirai Indian Ocean Cruise for the Study of MJO-Convective Onset (MISMO; Yoneyama et al. 2008). The Manus Island 2DVD has been operational since December 2011 (the data record examined herein is from 2 December 2011 to 21 April 2013; no continuous radar data are available at Manus). An identical 2DVD was operating on Gan Island 8 km away (141° radial) from the NCAR S-band dual-polarization (S-Pol) radar (Addu Atoll) during the 2011–12 Dynamics of the MJO field campaign (DYNAMO; Fig. 1; Yoneyama et al. 2013; Johnson and Ciesielski 2013). The Gan 2DVD and S-Pol radar operated simultaneously from 1 October 2011 to 16 January 2012; the Gan 2DVD record continues to 2 February 2012. Island conditions are considered to be similar to the surrounding ocean (Johnson and Ciesielski 2013).

Zuluaga and Houze (2013) describe the S-Pol radar deployment during DYNAMO and subsequent post-processing. S-Pol vertical cross section, or range height indicator (RHI), scans were collected directly over the Gan Island disdrometer every 15 min. Low-level plan position indicator (PPI) scans also captured the horizontal distribution of precipitation at the same time as the vertical cross sections. Radar scans were manually investigated. We use the horizontal reflectivity Z_h (dBZ), differential reflectivity Z_{dr} (positive for oblate, negative for prolate, and near zero for spherical or tumbling hydrometeors), and the correlation coefficient ρ_{hv} [a scalar quantity, decreases from unity because of the presence of non-Rayleigh scatterers and as hydrometeors in the same radar gate become less similar, either in phase, shape, and/or orientation; see Straka et al. (2000), BC01, and Kumjian (2013)]. Radar brightband identification caused by melting

snow is much more reliable with dual-polarization radar variables than with radar reflectivity alone (e.g., Brandes and Ikeda 2004; Thompson et al. 2014). The radar bright band is an indicator of stratiform rain type.

Unfortunately, we cannot analyze radar statistics of convective, stratiform, or total rainfall occurrence/accumulation over the disdrometer from PPI, RHI, or gridded horizontal reflectivity scans for a variety of reasons. The radar was blocked to the west, rendering echoes at low levels in this direction untrustworthy. The radar was also prohibitively close to the disdrometer, which placed the 2DVD within the "cone of silence" of gridded PPI radar reflectivity fields in the lower 3 km. Additionally, RHIs were not conducted south or west of the disdrometer location and were contaminated by ground clutter surrounding the disdrometer below 1 km. Therefore, horizontal reflectivity gradients and echo evolution cannot be assessed with either the PPI or RHI radar data within a 10-km radius surrounding the 2DVD, as specified by the Steiner et al. (1995) and Yuter and Houze (1998) radar-based C/S partitioning methods. Select RHIs were manually investigated over the disdrometer, but quantitative rainfall estimation above the 2DVD for all RHIs could not be conducted for statistical comparison with the 2DVD. Last, there is no established way to automatically classify C/S echoes with RHI or PPI polar coordinate radar data.

b. 2DVD data

Schönhuber et al. (2008) described the third-generation 2DVD in detail. The Department of Energy's Atmospheric Radiation Measurement Program (ARM) 2DVDs at Gan and Manus Islands provide 1-min drop count and drop number density[1] measurements across fifty 0.2-mm-wide-diameter bins ranging from 0.0–0.2 to 9.8–10.0 mm (http://www.archive.arm.gov/discovery/). Only 1-min DSD data with at least 100 total drops and $R > 0.05\,\mathrm{mm\,h^{-1}}$ during at least a 3-min consecutive raining period were analyzed. These thresholds prevent DSDs composed of only a few small drops from skewing the analysis (P. L. Smith and V. N. Bringi 2012, personal communication) and are consistent with our intent to focus on raining DSD. The 18-month Manus Island time series provided 27 179 one-minute raining DSD data points, while Gan Island had 4446 points over 3.5 months. No smoothing or averaging was performed. Besides the spatial sampling issues of a $100\,\mathrm{cm^2}$ area on the ground and some missed data during high winds, the chief 2DVD instrument error is the underestimation of small drops, so we ignored data from the first size bin centered on 0.1 mm, as suggested by Tokay et al. (2013). The 2DVDs directly sense integral[2] rain parameters, such as liquid water content LWC ($\mathrm{g\,m^{-3}}$) and rain rate R ($\mathrm{mm\,h^{-1}}$), the latter equivalent to the flux of water across the catchment area ($100\,\mathrm{cm^2}$) given each drop's measured fall speed. In contrast, Joss–Waldvogel impact disdrometers (JWDs) require drop count correction and calibration algorithms (Tokay et al. 2001, 2005, 2013), used to have worse small-drop detection capability, and must rely on an empirical fall speed relation based on drop diameter to calculate R and LWC (Gunn and Kinzer 1949; Atlas et al. 1973), which introduces additional error, as described by Salles and Creutin (2003).

A drop size distribution shape or model must be chosen when solving for the remaining integral rain parameters. Rainfall and radar quantities are heavily influenced not just by particle size, but also by the distribution of mass or water content across the particle size distribution [i.e., the median drop diameter D_0 (mm)]. DSDs naturally exhibit a gamma-shaped distribution (Ulbrich 1983), which can be normalized so DSDs of varying LWC can be easily compared (Willis 1984). For this reason, Lee et al. (2004) stated that normalized gamma DSD methods may produce more evident distinction between C/S rain types. Thurai et al. (2014) detailed the "μ search" method used in the current study to determine the normalized gamma DSD generalized number concentration[3] or intercept parameter N_w ($\mathrm{mm^{-1}\,m^{-3}}$) and shape parameter μ, from which D_0 is estimated. These parameters are related by

$$N_w = \frac{3.67^4 10^3 \mathrm{LWC}}{\pi \rho_w D_0^4}, \tag{1}$$

where ρ_w is the density of water, $1\,\mathrm{g\,cm^{-3}}$ (BC01). This μ-search technique is more accurate than the often-used method of moments because it takes more DSD information into account and iteratively seeks the gamma parameters that most likely describe the distribution of interest through minimization of cost functions (Smith and Kliche 2005; Kliche et al. 2008). For simplicity, $\log_{10} N_w$ is analyzed in the current study as in BR03.

c. Simulated radar variables

Surface disdrometer DSD data can be integrated to determine how a radar would sample that volume of

[1] Number of drops per diameter bin per unit volume of air ($\mathrm{mm^{-1}\,m^{-3}}$).

[2] Integral rain parameters are those found by integrating the DSD (Ulbrich and Atlas 1978).

[3] The normalized gamma number concentration or intercept parameter N_w is the same as that for an exponential-shaped distribution N_0 with equal LWC and D_0 to the gamma-shaped DSD. Note, N_w is different from the nonnormalized gamma intercept parameter (also denoted by N_0) used by Ulbrich (1983), Tokay and Short (1996), and Ulbrich and Atlas (1998). This N_0 still depends on the shape parameter μ, leading to less physical units of $\mathrm{mm^{-1}\,m^{-3}}\,\mu^{-1}$.

rain and to calibrate radar-based rainfall estimates (Waterman 1971; Mishchenko et al. 1996). It is necessary to compute radar reflectivity Z_h [(dBZ) or more often the linear version z (mm^6 m^{-3}) because of its larger dynamic range] based on theoretical, electromagnetic scattering calculations from the raw DSD number density data rather than using the simplified $z \sim D^6$ calculation for spheres, which ignores the effects of drop oblateness and fall behavior. Radar reflectivity was simulated assuming rain drops were liquid, had a zero mean canting angle with a standard deviation about the mean up to 7.5° (Huang et al. 2008), and followed the Thurai et al. (2007) drop shape model. Drops were considered to be 20°C and viewed at a nearly horizontal (1°) incident angle at S band (11 cm; e.g., S-Pol). Since Z_h should be independent of wavelength for Rayleigh scatterers, S-band $R(z)$ equations can be applied to C- and X-band data. We use orthogonal linear regression to derive all power-law equations, including $R(z)$, because it minimizes error in both the R and z directions perpendicular to the best-fit line, so $R(z)$ and $z(R)$ are equivalent.

3. Drop size distribution observations

To investigate DSD variability at Gan and Manus Islands, D_{MAX}, D_0, $\log_{10}N_w$, and LWC histograms normalized by the length of each dataset are shown in Fig. 2. Table 1 shows that the Gan and Manus Island datasets exhibit similar variances, means, standard deviations, minima, maxima, and 5th and 95th percentiles of D_{MAX}, D_0, LWC, and $\log_{10}N_w$ (Table 1). Most D_{MAX} values at both locations are between 1.0 and 3.6 mm. The LWC values are near ~0.03–0.1 g m^{-3}, but some values exceed 5 g m^{-3}, indicative of strong cumulonimbus clouds (Cotton et al. 2011).The D_0 values are small (0.8–1 mm), but large D_0 values >1.6 mm are observed. Potentially related to the issue of small drop detection by older instruments, many previous tropical oceanic DSD studies except Bringi et al. (2012) list slightly higher mean D_0 (Table 2). The LWC, D_{MAX}, and D_0 are slightly higher at Manus compared to Gan Island, with slightly lower $\log_{10}N_w$, which is also evident in Fig. 2. Despite these minimal differences and being separated by the Maritime Continent, DSD distributions at Manus and Gan Islands still appear very similar, suggesting that the cloud microphysical processes in these two regions are analogous or nearly equivalent. Many studies have shown similar cloud population intensity, morphology, and radar echo evolution over each tropical ocean basin associated with the ITCZ and MJO (Short et al. 1997; LeMone et al. 1998; DeMott and Rutledge 1998a,b; Rickenbach and Rutledge 1998; Zuluaga and Houze 2013; Barnes and Houze 2013;

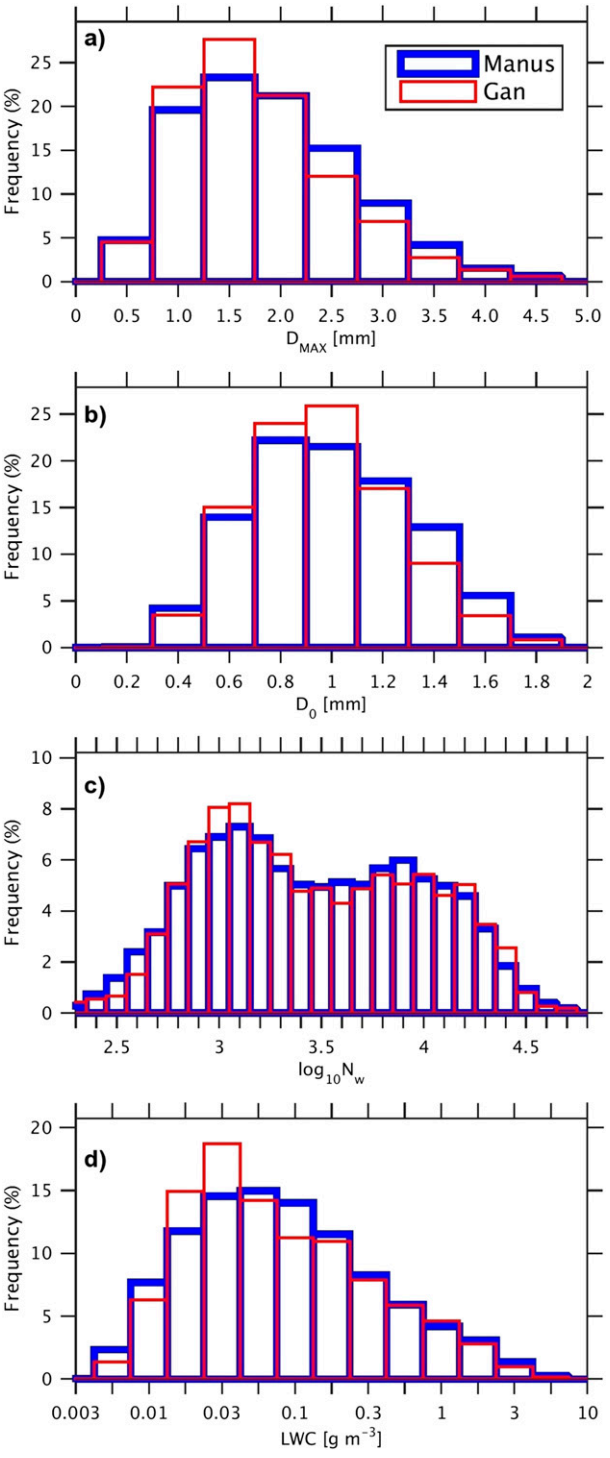

FIG. 2. Histograms normalized by record length for Manus and Gan 2DVD DSD (a) max diameter D_{MAX} (mm), (b) median diameter D_0 (mm), (c) number concentration $\log_{10}N_w$ (unitless), and (d) liquid water content LWC (g m^{-3}, binned on a $\log_{10}$ scale).

TABLE 1. Variance (var), mean, standard deviation, min, max, and 5th and 95th percentiles of integral rain parameters at Manus (27 142 points) and Gan (4446 points) Islands: DSD max diameter D_{MAX} (mm); median diameter D_0 (mm); liquid water content LWC (g m^{-3}); number concentration $\log_{10}N_w$ (unitless).

Place	Parameter	Var	Mean	Std dev	Min	5%	95%	Max
Manus	D_{MAX}	0.73	2.16	0.85	0.80	1.00	3.66	8.54
Gan	D_{MAX}	0.69	2.06	0.83	0.80	1.01	3.55	7.61
Manus	D_0	0.11	1.11	0.33	0.34	0.61	1.65	3.83
Gan	D_0	0.10	1.08	0.32	0.35	0.62	1.62	3.35
Manus	LWC	0.58	0.35	0.76	0.00	0.01	1.72	12.64
Gan	LWC	0.43	0.32	0.65	0.01	0.02	1.56	8.75
Manus	$\log_{10}N_w$	0.28	3.70	0.53	1.57	2.89	4.55	5.22
Gan	$\log_{10}N_w$	0.29	3.72	0.54	1.97	2.95	4.59	5.57

Xu and Rutledge 2014, 2015; Guy and Jorgensen 2014; Rowe and Houze 2014).

The mean $\log_{10}N_w$ for both sites is about 3.7 (Table 1 and Fig. 2), which is close to the Marshall and Palmer (1948) exponential DSD concentration, $\log_{10}(8000)\,\text{m}^{-3}\,\text{mm}^{-1} = 3.9$, as well as to the mean values listed in Table 2 found by BC01, Illingworth and Blackman (2002), TH10, Islam et al. (2012), and Penide et al. (2013). The mean $\log_{10}N_w$ lies between bimodal distribution peaks at about 3.25 and 4.1, which are nearly one standard deviation (σ) from the mean and almost 2σ from each other. These bimodal $\log_{10}N_w$ peaks correspond to an order-of-magnitude difference in number concentration (N_w). Bimodal $\log_{10}N_w$ probability distribution function (PDF) peaks at other maritime locations were also found by Ulbrich and Atlas (2007), BR09, TH10, and Bringi et al. (2012) corresponding to maritime stratiform and convective populations (Table 2). Tokay and Short (1996) and Testud et al. (2001) also documented two C/S modes with higher number concentration, LWC, and DSD slope (λ for exponential DSD) for a given rain rate in convection compared to stratiform. This reflects the fact that stratiform rain has been affected by aggregation above and in the melting layer, which shifts mass to larger size bins, reduces number concentration, and also flattens the DSD slope (Lo and Passarelli 1982). In accordance with these previous studies, we suggest that a physically based distinction between convective and stratiform rain produced the $\log_{10}N_w$ bimodality observed in Fig. 2 for Gan and Manus Islands.

BR03 and BR09 plotted $\log_{10}N_w$ against D_0 to distinguish different modes of raining DSD variability. They found a sloped separator line at $\log_{10}N_w^{SEP} = -1.6D_0 + 6.3$, where convective storms existed to the right of (above) the separator line. They considered mostly strong coastal tropical, coastal subtropical, and continental midlatitude convection. Stratiform rain was nearly always situated to the left of (below) their separation line, with decaying convection, or convection transitioning into stratiform rain, extending into the high $\log_{10}N_w$, low D_0 quadrant. TH10 investigated maritime convection and stratiform rain and found them separated by the same BR09 line, but with variations in $\log_{10}N_w$ playing a significant role. They also presented weak, maritime convective DSD sample means of several thousand data points from Okinawa, Japan, that were just below the BR09 line at high $\log_{10}N_w$ but relatively low D_0, suggestive of maritime, warm rain processes.

Figure 3 shows $\log_{10}N_w$ and D_0 smoothed 2D histograms for Gan and Manus Islands. The relatively sharp cutoff of data in the lowest $N_w(D_0)$ quadrant is due to necessary rain

TABLE 2. Mean values of median diameter D_0 (mm) and number concentration $\log_{10}N_w$ (unitless) from previous studies of all, convective, and stratiform rain in tropical, maritime locations.

Source	Rain	Mean D_0	Mean $\log_{10}N_w$
Penide et al. (2013) Australia monsoon	All	1.5	3.7
Islam et al. (2012) United Kingdom	All	1.23	3.7
BC01 Australia monsoon	All	1.20	3.7
Bringi et al. (2012) Kwajalein	All	0.9	—
Tokay and Short (1996) TOGA COARE	C	1.24	—
Ulbrich and Atlas (1998) TOGA COARE	C	0.8–1.0	—
Tokay et al. (1999) TOGA COARE	Deep C	1.31	—
Tokay et al. (1999) TOGA COARE	Shallow C	1.22	—
Testud et al. (2001) TOGA COARE	C	1.3–1.5	—
BR03 Florida	C	1.6	4.6
Ulbrich and Atlas (2007) Maritime	C	1.3–1.7	4.3
BR09 Australia monsoon	C	1.44	4.2
TH10 Australia monsoon	C	1.00	4.6
TH10 Okinawa	C	1.05	4.6
Bringi et al. (2012)	C	—	3.9
Tokay and Short (1996) TOGA COARE	S	1.61	—
Tokay et al. (1999) TOGA COARE	S	1.54	—
Testud et al. (2001) TOGA COARE	S	1.3	—
BR09 Australia monsoon	S	1.22	3.5
TH10 Australia monsoon	S	1.35	3.3
Bringi et al. (2012) Kwajalein	S	—	3.47

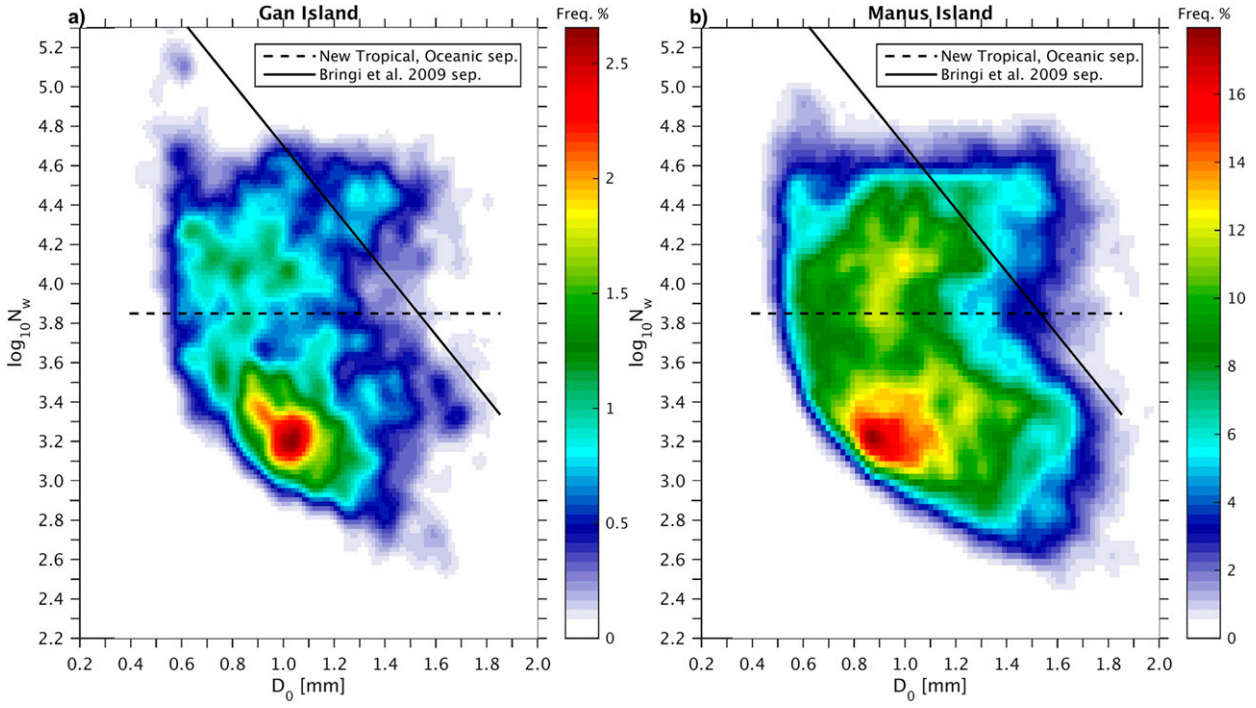

FIG. 3. Gan and Manus Island $N_w(D_0)$ smoothed 2D histograms contoured by frequency of occurrence with the original subtropical, continental BR09 $\log_{10}N_w^{\mathrm{SEP}} = -1.6D_0 + 6.3$ and updated tropical, oceanic C/S $\log_{10}N_w = 3.85$ separation lines. Gan (Manus) Island: 130 (100) bins in each direction; 13 (8) bin Gaussian filter width.

rate and total drop number data quality thresholds. The Manus samples are more numerous and more evenly spread but distributed in similar spatial orientations compared to the Gan samples, as suggested by the histograms of individual parameters in Fig. 2. A large proportion of data exists near $\log_{10}N_w = 3.2$ and $D_0 = 1.0$ mm (Gan) and 0.9 mm (Manus), corresponding to stratiform rain in BR03, BR09, and TH10. A secondary peak occurs near $\log_{10}N_w = 4.1$ and $D_0 = 0.7$–1.1 mm, similar to the shallow, weak, convective Okinawa data from TH10. These two frequent modes of variability appear to be separated by a nearly horizontally oriented area of lower frequency of occurrence somewhere between $\log_{10}N_w = 3.7$ and 3.9. Figure 3 shows that a very small fraction of the Manus and Gan Island data points would be classified as convective by the BR09 separator line, which does not seem to fall between any natural breaks in this tropical, maritime $N_w(D_0)$ distribution. Although Barnes and Houze (2014) and Rowe and Houze (2014) show radar observations of graupel and small hail aloft in storms during DYNAMO in the central Indian Ocean, which result in high D_0 and low $\log_{10}N_w$, these vigorous convective processes are not frequent over the warm pool and certainly not to the same magnitude as the midlatitude and subtropical continental convection considered when forming the BR09 separation line. Instead, a new convective/stratiform separator line at $\log_{10}N_w^{\mathrm{SEP}} = 3.85$ is drawn for this unique tropical, oceanic dataset, bifurcating the two modes of variability in Fig. 3. The placement of this line will be verified by extensive case study analysis in section 4 and mathematically tested in section 5.

It is worth pointing out that the $\log_{10}N_w^{\mathrm{SEP}}$ line drawn in Fig. 3 is mathematically equivalent to $\mathrm{LWC}^{\mathrm{SEP}} = 0.1226D_0^4$ through Eq. (1). The corresponding LWC(D_0) distributions for the Gan and Manus Islands also exhibit two modes of variability on either side of this separator line (Fig. 4), each oriented in the same direction of increasing LWC for increasing D_0 when both variables are plotted on a logarithmic scale [illustrating the LWC $\sim D_0^4$ dependence in Eq. (1)]. As seen for $N_w(D_0)$, the LWC(D_0) distributions at each location also appear very spatially correlated, except that the Gan Island dataset has fewer total data points so that the contoured 2D histogram clusters are not as well organized as for Manus Island. The 2D histograms of LWC(D_{MAX}) also exhibit two modes of variability, similar to LWC(D_0).

Using Figs. 3 and 4 as references, the next section is devoted to 1) explaining why these two frequency peaks, in both the $N_w(D_0)$ and LWC(D_0) spaces, actually correspond to stratiform and convective tropical, oceanic rain and 2) justifying the placement of the new $\log_{10}N_w^{\mathrm{SEP}}$ separation line.

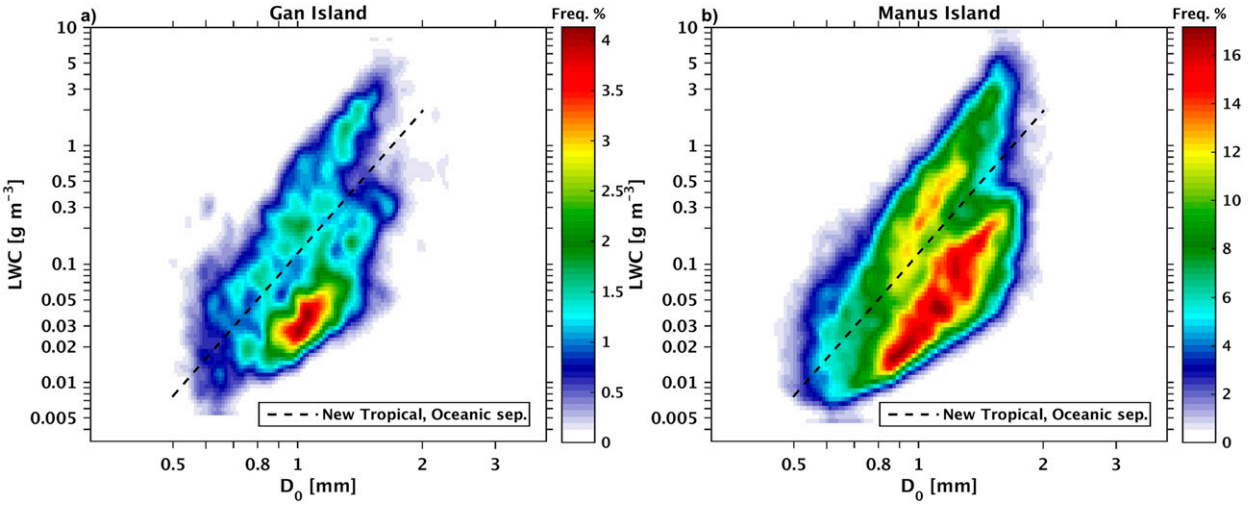

FIG. 4. Gan and Manus Island LWC(D_0) smoothed 2D histograms contoured by frequency of occurrence with the updated tropical, oceanic C/S rain LWC$^{\mathrm{SEP}}$ separation line, which is equivalent to $\log_{10}N_w^{\mathrm{SEP}} = 3.85$. Gan (Manus) Island: 105 (100) bins in each direction; 4 (2) bin Gaussian filter width.

4. Radar observations

The entire DYNAMO S-Pol RHI dataset was examined to find times when the radar indicated rain over the disdrometer and the disdrometer also recorded data. This resulted in 372 analyzed case studies of S-Pol vertical cross section radar scans with coincident Gan Island 2DVD data. Analyzing sequences of paired observations helped elucidate the evolution of DSD spectra with respect to the horizontal and vertical evolution of radar echoes above and around the disdrometer. These case studies reveal why a separation line at $\log_{10}N_w^{\mathrm{SEP}} = 3.85$ can be drawn to delineate convective and stratiform rain encountered at Manus and Gan Islands. Of the 372 case studies analyzed, 9 are presented in this section. They are representative cases spanning the entire $N_w(D_0)$ and LWC(D_0) parameter spaces and, thus, the full intensity and organizational spectrum between stratiform and tropical, maritime convective rain. Note that the 0°C level was consistently between 4.5 and 5.1 km AGL (550–600 hPa) during these DYNAMO case studies. Residual ground clutter (identifiable by low ρ_{hv} and negative/variable Z_{dr}) contaminates radar data near the disdrometer (varying from case to case depending on atmospheric refraction of the radar beam downward).

a. Case 1: Strong, widespread convection

Figure 5 shows an example of widespread, deep convection. The S-Pol radar horizontal (PPI) and vertical (RHI) cross sections over the Gan disdrometer, 8 km away at 141° azimuth, show a large area of $Z_h > 50$ dBZ over the disdrometer and extending up to 5.5 km AGL. The differential reflectivity over the disdrometer is over 2 dB, indicating the presence of large, horizontally oriented raindrops (BC01). High Z_{dr} of this same magnitude and low ρ_{hv} to 0.93 near 5 km AGL indicates some melting, but in a disrupted fashion because of strong convection. A horizontally elongated, stable, stratiform rain radar bright band is not evident. As this deep convection passed over the disdrometer, $\log_{10}N_w$ and D_0 were both relatively high, between 4.3 and 4.6 and 1.4 and 1.7 mm, respectively. The LWC was correspondingly high, with values approaching 5 g m^{-3}, and rain rates were between 30 and 100 mm h^{-1}. The BR09 method would have classified this example as convection.

b. Case 2: Strong, isolated convection

Figure 6 shows another case of strong convection with near-surface reflectivity exceeding 45 dBZ, but associated with an isolated cell. The Z_{dr} is above 1 dB below 2 km, and ρ_{hv} is above 0.99 throughout the entirety of the echo, meaning there is no established melting layer. The number concentration ($\log_{10}N_w$) is slightly lower than the widespread deep convective case in Fig. 5, between 4.0 and 4.2. Since N_w is proportional to LWC by Eq. (1), it is not surprising that LWC for this case is also slightly lower, near 2–4 g m^{-3}, while rain rates were between 30 and 50 mm h^{-1}. However, the median drop diameters of these DSDs are slightly higher than case 1, exceeding 1.5 mm. Both the widespread and isolated strong convective cases are near the upper, right-hand edge of the $N_w(D_0)$ and LWC(D_0) 2D histograms (Figs. 3 and 4). The BR09 method would have classified this example as convection.

c. Case 3: Weak, widespread convection

Weaker convection was frequently observed according to DSD and radar observations. This type of weakly

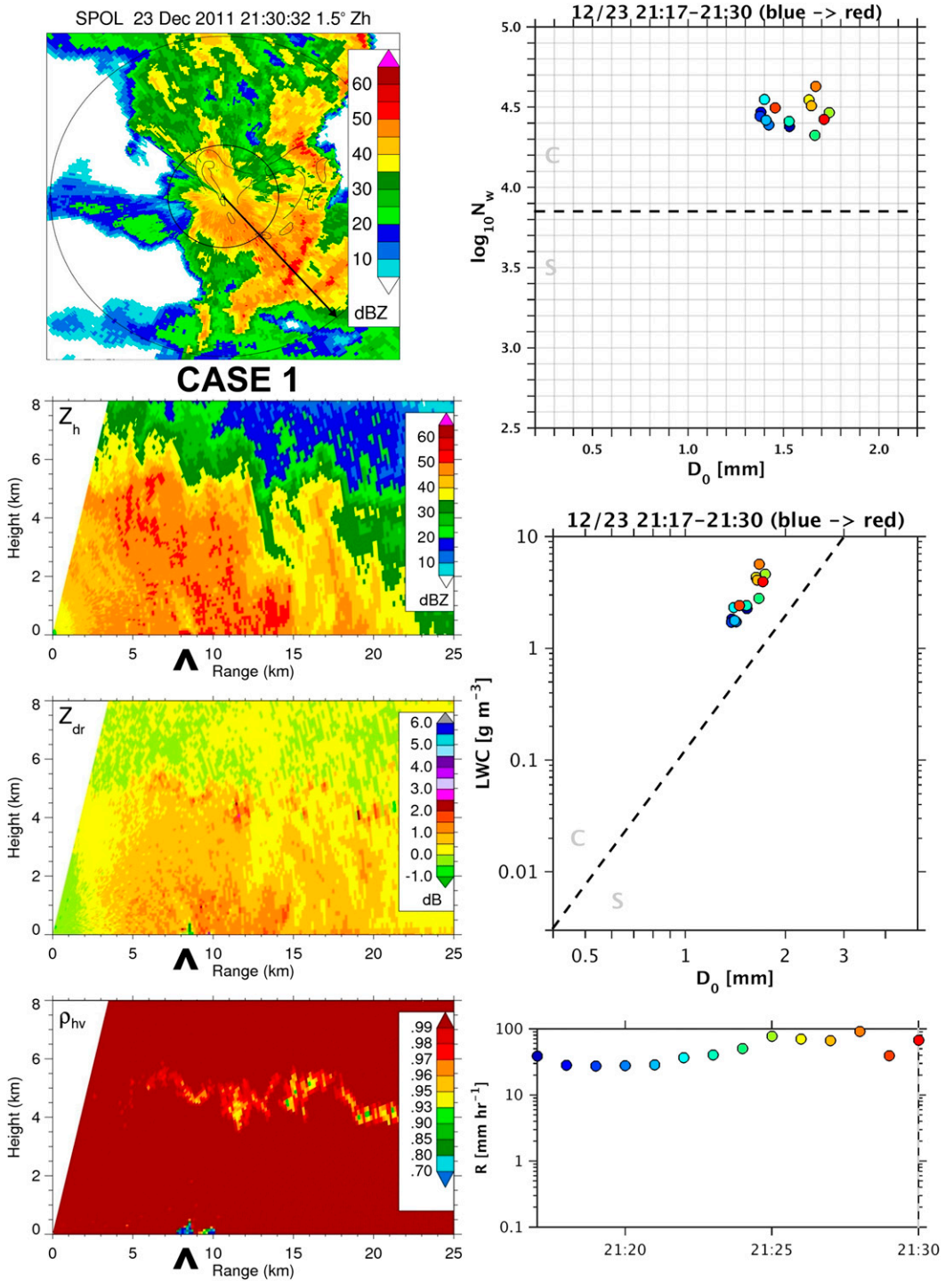

FIG. 5. Case study 1 of widespread deep convection at 2130 UTC 23 Dec 2011 with S-Pol radar PPI and RHI of reflectivity Z_h, differential reflectivity Z_{dr}, and the correlation coefficient ρ_{hv}. Range rings at 8 and 25 km; Gan Island 2DVD along the black arrow at 8-km range denoted by the caret on RHI in this direction. The $N_w(D_0)$, LWC (D_0), and R time series are plotted throughout 2117–2130 UTC, where time increases as the colored markers go from blue to red. The $\log_{10}N_w^{SEP}$ separation line and its equivalent LWC^{SEP} line are plotted to differentiate convection above and stratiform rain below.

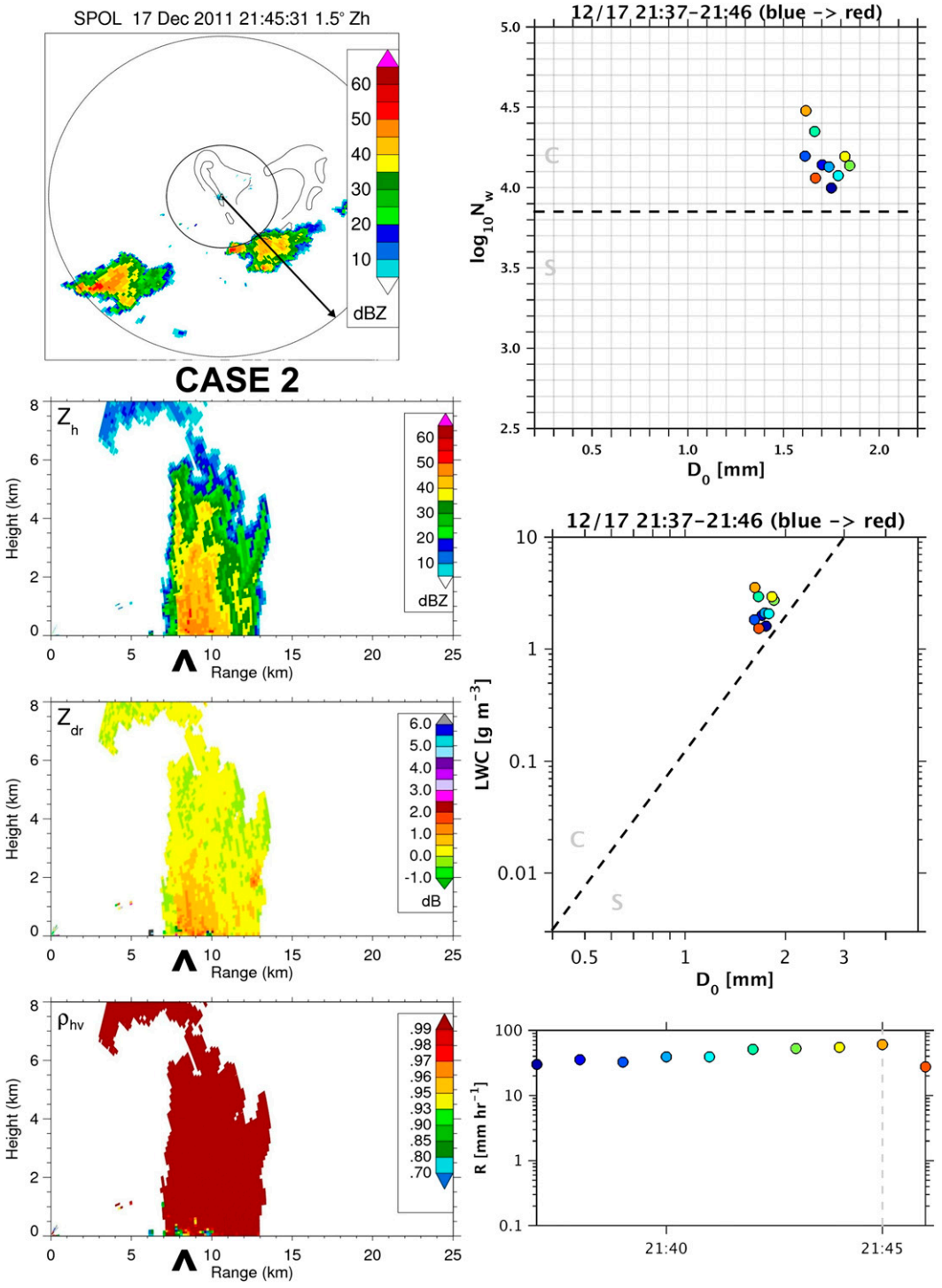

FIG. 6. Case study 2: as in Fig. 5, but for isolated strong convection at 2145 UTC 17 Dec 2011, with 2DVD data spanning 2137–2146 UTC. Time increases as the colored markers go from blue to red.

forced, weakly organized convection tended to decay rapidly. Figure 7 is an example of localized enhancements of reflectivity extending from the surface upward that, according to radar vertical cross sections, do not even reach the 0°C level (4.5–5.1 km AGL or 600–550 hPa throughout the field campaign). Therefore, these warm rain DSDs could not have been influenced by vapor deposition, aggregation, or

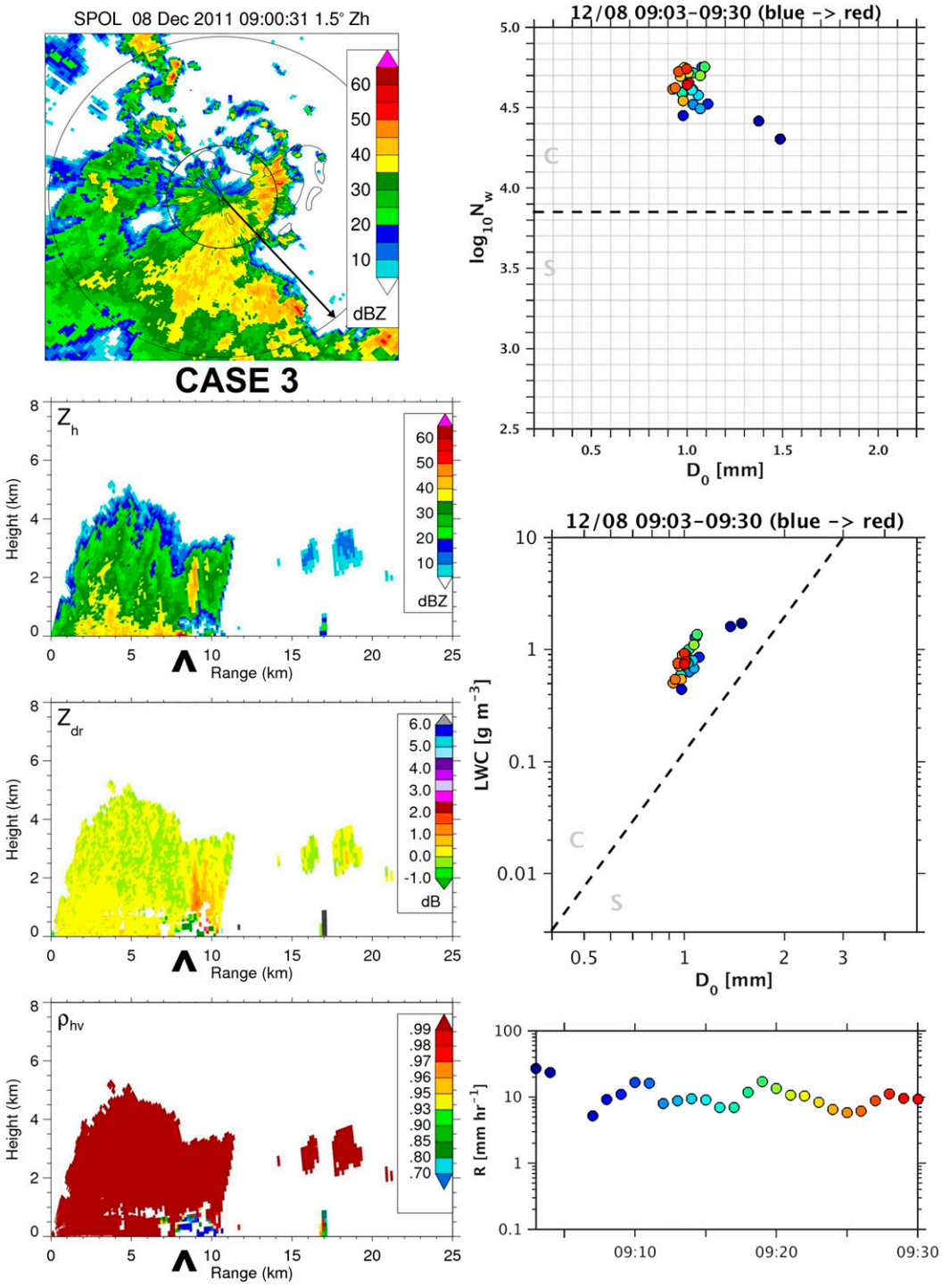

FIG. 7. Case study 3: as in Fig. 5, but for widespread, shallow convection at 0900 UTC 08 Dec 2011, with 2DVD data spanning 0903–0930 UTC. Time increases as the colored markers go from blue to red.

melting. This case is thus convective in nature, driven by surface buoyancy. The Z_{dr} is near zero, and ρ_{hv} is near unity throughout most of this shallow echo except for the leading edge at the beginning of the time series (storm propagated southeast over the 2DVD). For more than 45 min after this initial radar scan, the $\log_{10}N_w$ remained relatively high near 4.6–4.8, while D_0 was near 1 mm, consistent with the lower radar

reflectivities seen in this example compared to stronger convection. LWC was still near 0.5–1 g m^{-3} on the top side of the LWC^{SEP} line with rain rates between 5 and 15 mm h^{-1}. DSDs in both parameter spaces were indicative of belonging to the upper mode of each bimodal distribution shown in the previous section. These DSDs lie directly on the BR09 separation line (not shown).

d. Case 4: Weaker, isolated convection

An example of even weaker, shallower convection in Fig. 8 shows the same high $\log_{10}N_w$ near 4.5 as the weak, widespread convection in case 3, but with D_0 as low as 0.6 mm. The LWC is correspondingly lower between 0.1 and 0.5 g m^{-3}, with R between 1 and 5 mm h^{-1}. These radar echoes are also smaller in horizontal area. Radar reflectivity is mostly between 20 and 30 dBZ, with some localized areas above 35 dBZ. The vertical elongation of these echoes upward, but only to 4 km AGL, and the lack of any radar signatures of melting, aggregation, or ice aloft signifies that these echoes are convective in origin, driven by buoyancy within the moist marine boundary layer. The continental, subtropical BR09 separation would have classified these DSD as stratiform.

e. Case 5: Weaker, shallower convection

At the highest $\log_{10}N_w$ but lowest D_0 end of the spectrum, light rain with echo tops below 2 km AGL was observed in several cases akin to Fig. 9. The shallow cloud depth, confined below the trade wind inversion in this case, likely played a role in limiting drop growth. The maximum diameters from these DSDs ranged from 0.83 to 1.98 mm, with an average maximum diameter of only 1.32 mm. Median drop diameters were 0.5–0.75 mm. These light rain DSDs account for the extension of the $N_w(D_0)$ 2D histogram in Fig. 3 up and to the far left of the diagram, which also lies on the stratiform side of the BR09 separation line. The radar characteristics and inferred low-level heating profile of this precipitation warrant its classification as convection, albeit weak. The Z_h remained below 30 dBZ, horizontal Z_h gradients were weak, Z_{dr} remained near zero, and ρ_{hv} was near unity, except for obvious ground clutter where $\rho_{hv} < 0.75$ and $Z_{dr} <$ 0.5 dB. As expected, rain rate was fairly low, ranging between 0.3 and 10 mm h^{-1}.

f. Case 6: Moderate stratiform

Moderate stratiform rain exhibits much different radar and DSD characteristics than convection (Houze 1997). For instance, stratiform rain in Fig. 10 has rain rates in the same ranges as the preceding weak convection ($<$10 mm h^{-1}), similarly low LWC between 0.1 and 0.5 g m^{-3}, but $D_0 > 1$ mm and $\log_{10}N_w$ between 3.6 and 3.85. The same R and LWC were apparently achieved with much lower $\log_{10}N_w$, slightly greater surface Z_h, and greater D_0. This suggests that these DSDs exhibit different covariances between the integral rain parameters compared to convection (Atlas et al. 1973). The LWC(D_0) and $N_w(D_0)$ points are on the stratiform side of the separation lines. Throughout inspection of all 372 radar–2DVD case studies, stratiform rain with a clear radar bright band was observed to approach, but stay below the $\log_{10}N_w^{SEP} = 3.85$ line. These DSDs were aligned with the stratiform rain distributions in BR03, BR09, and TH10, suggesting that the stratiform $N_w(D_0)$ ranges are not as region dependent as convection.

g. Case 7: Weak stratiform

Widespread, weaker stratiform rain (Fig. 11) exhibited brightband signatures but with even lower surface $\log_{10}N_w$ near 3.3 and $D_0 < 1$ mm, consistent with lower surface Z_h. The LWC(D_0) samples during this time were on the lower side of the LWC^{SEP} line, with R only ranging from 0.1 to 0.3 mm h^{-1}. These samples were nearly coincident with the main frequency of occurrence maxima observed in Figs. 3 and 4. This mode of precipitation is obviously more frequently observed than the upper mode of LWC(D_0) and $N_w(D_0)$ variability associated with convection, most likely because stratiform rain lasts longer and covers a wider area. This is consistent with previous tropical rainfall studies that report stratiform rain being more commonly observed per unit area and per unit time than convection, even though convection is responsible for more accumulated rainfall (e.g., Cheng and Houze 1979; Tokay and Short 1996; Zuluaga and Houze 2013; Xu and Rutledge 2014). The BR09 method would have classified these echoes as stratiform.

h. Case 8: Gradual transition from embedded convection to stratiform

The last two case studies demonstrate convection transitioning to stratiform rain. Figure 12 begins with convection embedded in a widespread, long-lived stratiform rain region. Low-level reflectivity exceeds 45 dBZ. The convective updrafts and precipitation growth processes appear to have disrupted the bright band locally above the disdrometer. The $\log_{10}N_w$ during this first scan of the series was well above the new separation line at 4.3, while D_0 was nearly 1.5 mm, R was near 30 mm h^{-1}, and LWC was just over 1 g m^{-3}. The second set of radar scans show that the

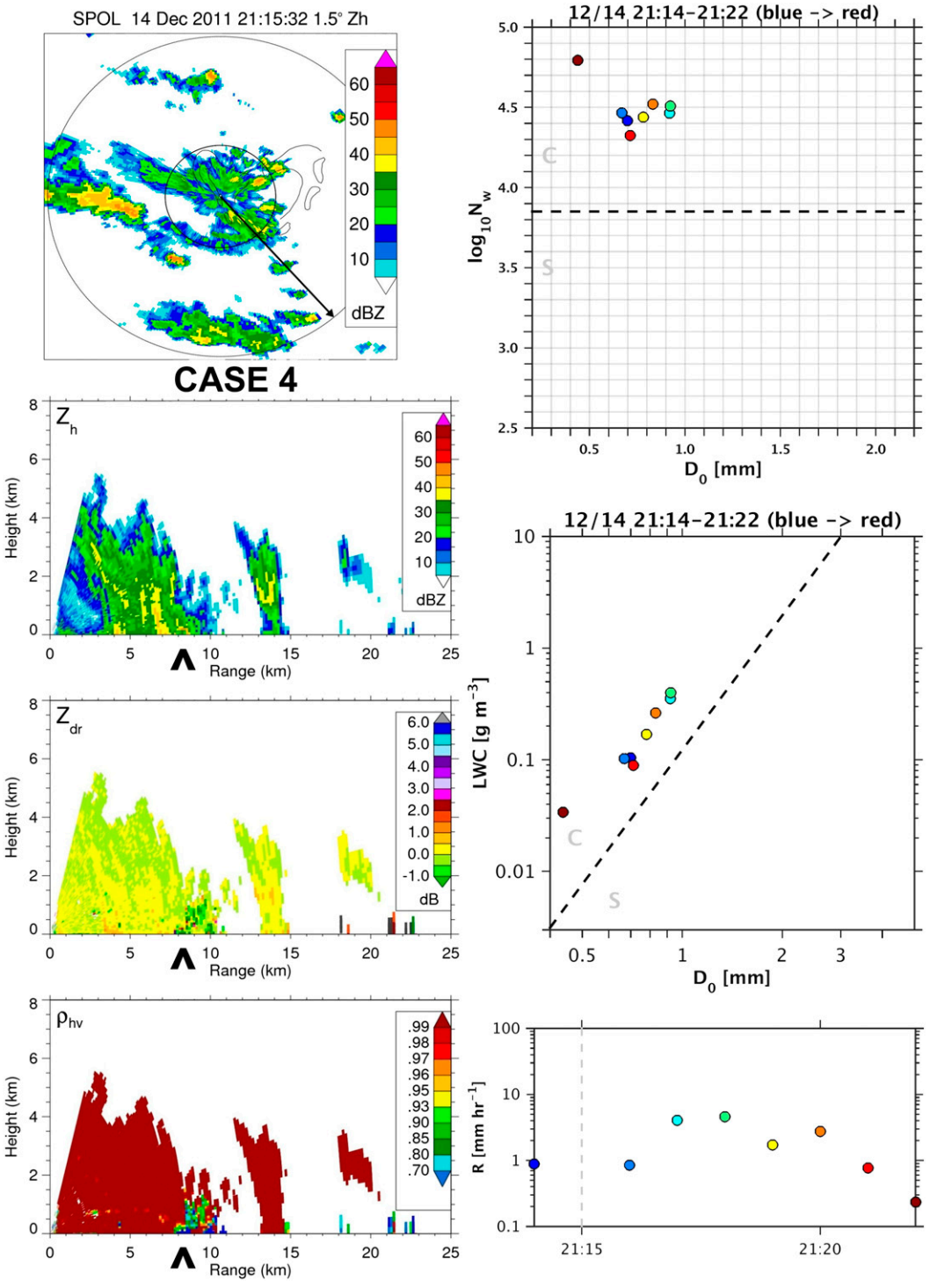

FIG. 8. Case study 4: as in Fig. 5, but for shallow convection at 2115 UTC 14 Dec 2011, with 2DVD data spanning 2114–2122 UTC. Time increases as the colored markers go from blue to red.

convection decayed over a 30-min period and the region of high reflectivity descended to the ground. The bright band also started to become more established and uniform during this time. However, there were still areas of enhanced reflectivity aloft, which were vertically elongated above the high-reflectivity fall streak. The DSDs remained on the upper portion of the $N_w(D_0)$ and LWC(D_0) distributions, but were

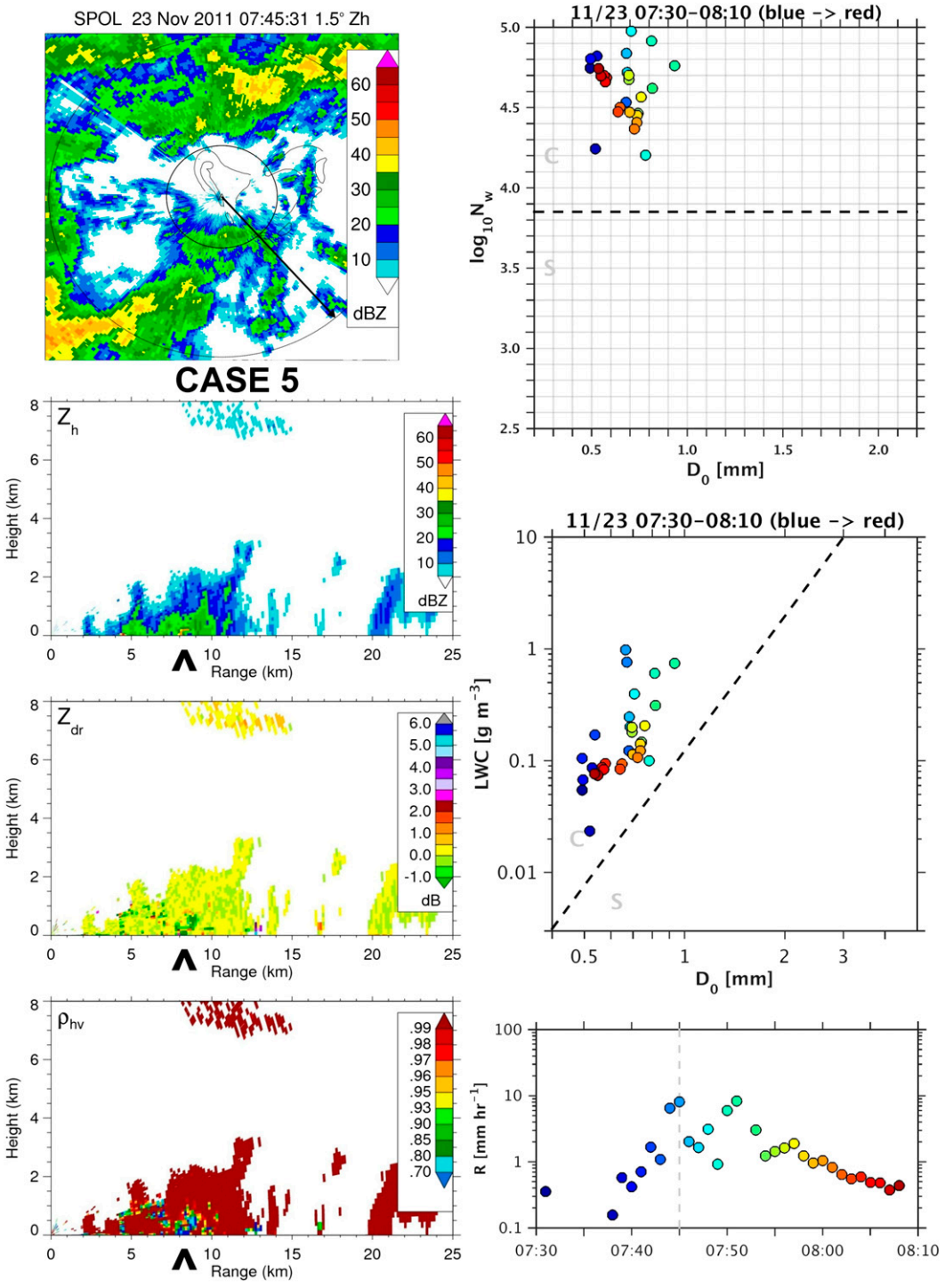

FIG. 9. Case study 5: as in Fig. 5, but for light rain at 0745 UTC 23 Nov 2011, with 2DVD data spanning 0730–0810 UTC. Time increases as the colored markers go from blue to red.

approaching each separation line. Likewise, rain rates were 10 mm h^{-1}.

By the time of the third radar scan 30 min later, 1 h after strong convection passed over the disdrometer, the radar echoes were more horizontally uniform, many portions of the radar bright band showed ρ_{hv} below 0.93, DSD had crossed the LWC(D_0) and $N_w(D_0)$ separation lines, and rain rates decreased to 3 mm h^{-1}. The fourth

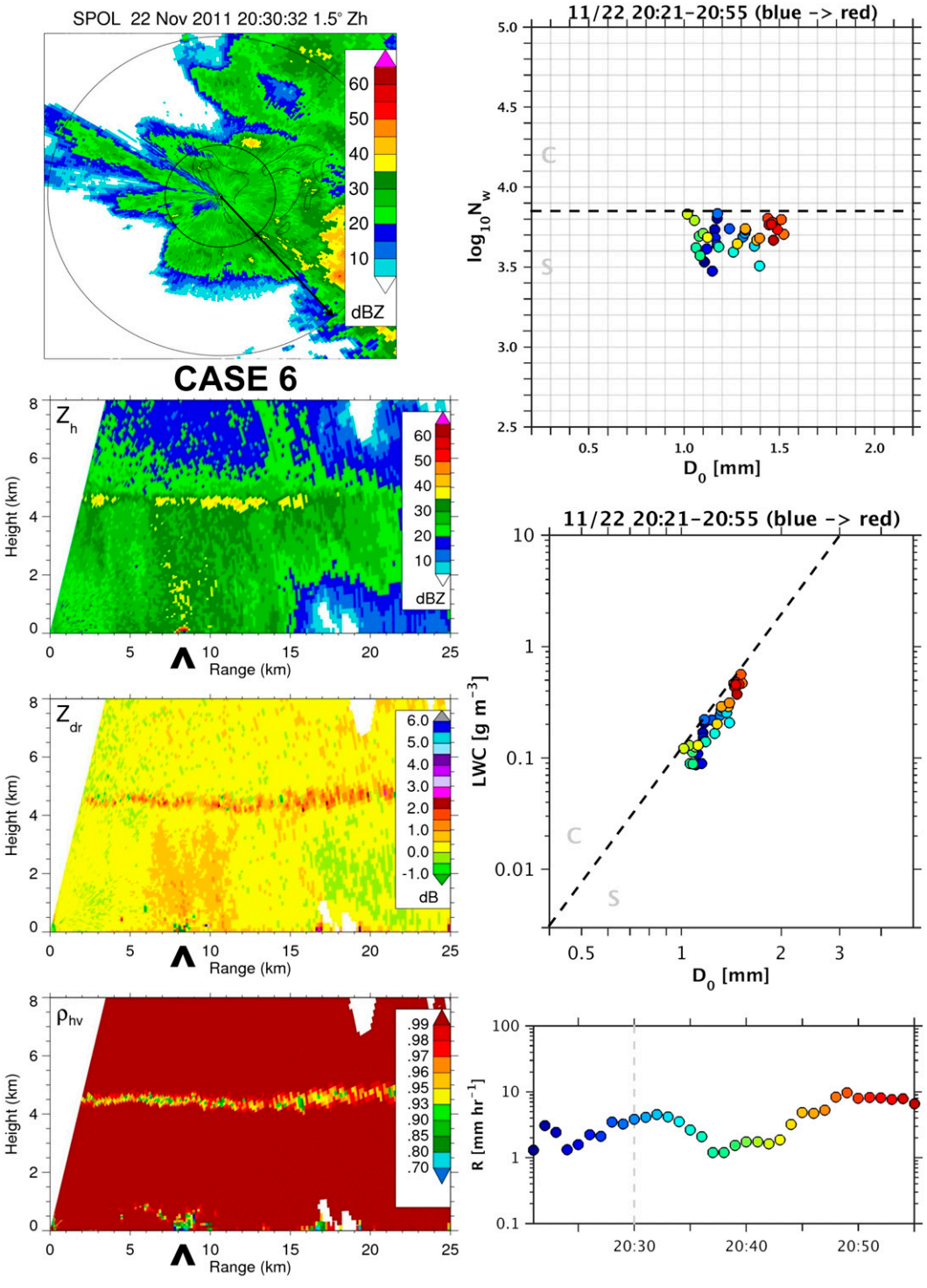

FIG. 10. Case study 6: as in Fig. 5, but for stratiform rain at 2031 UTC 22 Nov 2011, with 2DVD data spanning 2021–2055 UTC. Time increases as the colored markers go from blue to red.

radar scan shows an invigoration of the radar bright band to above 45 dBZ over a +15-km-wide area near 4.5 km AGL. A deep portion of the radar bright band exhibited $\rho_{hv} < 0.83$ and $Z_{dr} > 2$ dB. These polarimetric data are consistent with the expectation of large rain drops at the surface (Tokay et al. 1999; Brandes et al. 2004), which was verified by observations of D_0 near 1.9 mm at this time. Near-surface Z_{dr} was 0.5–1 dB, and

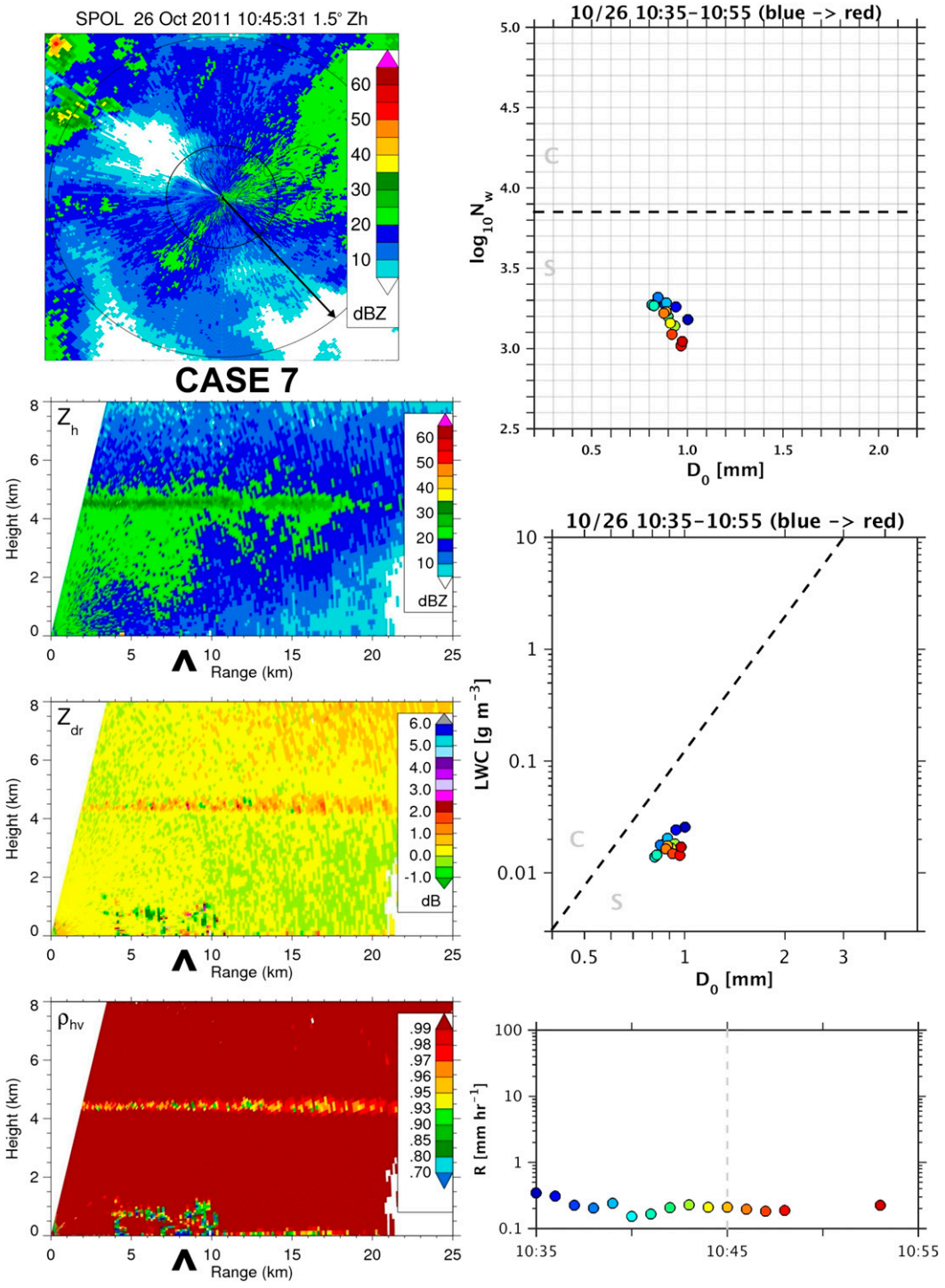

FIG. 11. Case study 7: as in Fig. 5, but for weak stratiform rain at 1045 UTC 26 Oct 2011, with 2DVD data spanning 1035–1055 UTC. Time increases as the colored markers go from blue to red.

surface rain rates were just under 10 mm h^{-1}. The layer of near-zero Z_{dr} just above the bright band and increasing Z_{dr} with altitude toward echo top above the disdrometer suggest pristine ice crystal growth near cloud top and subsequent aggregation above the melting layer (Ryzhkov et al. 2005; Kennedy and Rutledge 2011; Thompson et al. 2014). Braun and Houze (1994) highlight the role of vapor deposition aloft in producing

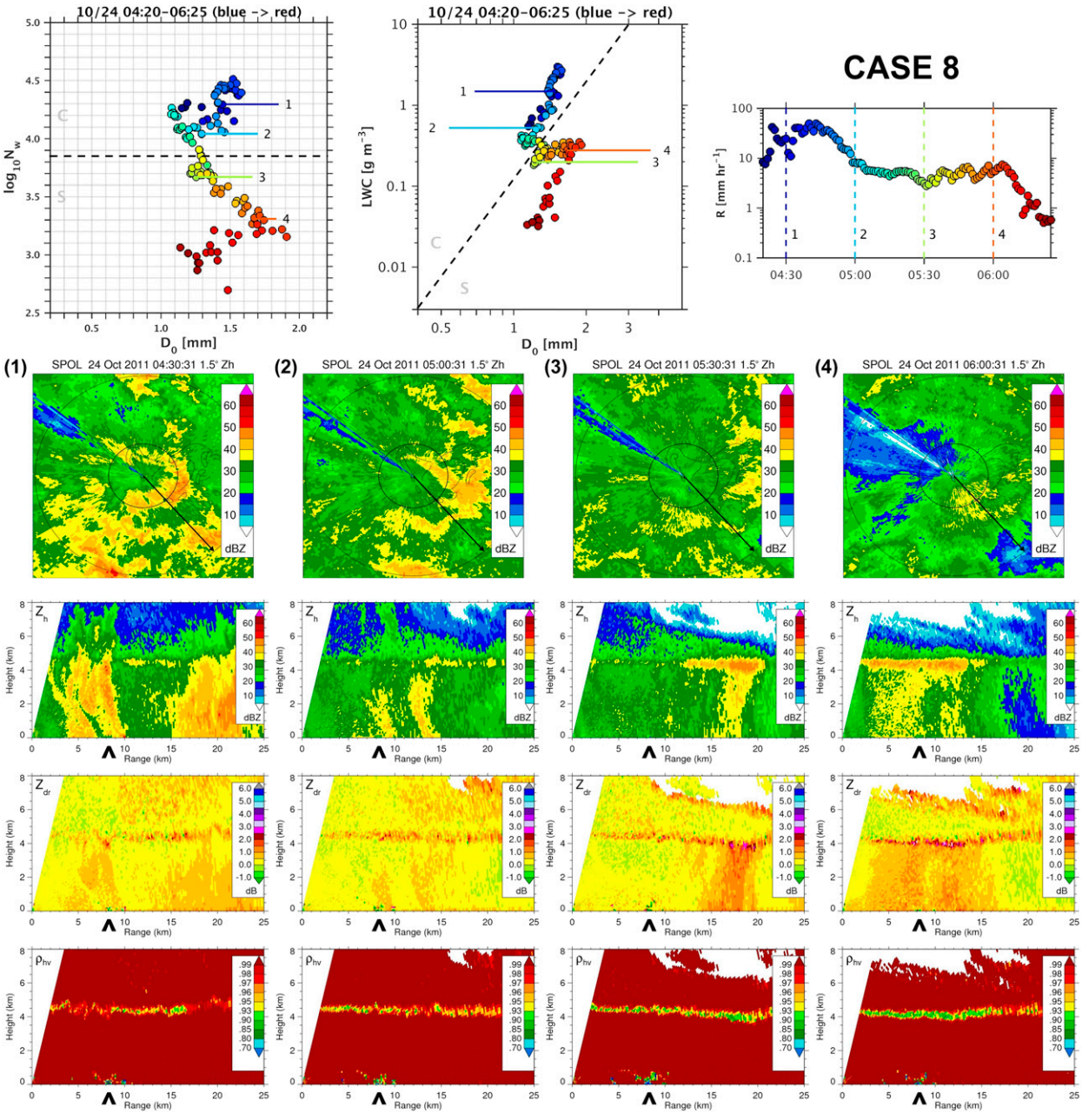

FIG. 12. Case study 8: as in Fig. 5, but for a transition from a leading convection line to strong stratiform rain at 0430, 0500, 0530, and 0600 UTC 24 Oct 2011 (corresponding to label numbers 1–4, respectively), with 2DVD data spanning 0420–0625 UTC. Numbers 1–4 correspond to callout points in the 2DVD data based on the time of the radar scans, where time increases as the colored markers go from blue to red.

strong stratiform bright bands. In addition, the aggregation process can concentrate LWC into fewer, but larger drops, which is supported by the trends observed in these DSD parameters from radar scans 2–4: lower LWC near 0.3 g m^{-3}, greater D_0, and lower $\log_{10}N_w$ near 3.2 compared to scans 2 and 3. This "zig–zag" migration through integral rain parameter spaces during a C/S transition was also noted by Tokay and Short (1996) and Atlas et al. (1999). The further decrease in surface D_0, LWC, R, Z_h, and even $\log_{10}N_w$ toward the end of this DSD sample period was associated with much lighter stratiform rain and a weaker bright band (not shown with radar, similar to case 7).

i. Case 9: Abrupt transition from leading convection to stratiform

A different but commonly observed transition from a leading convective line to a trailing stratiform region is

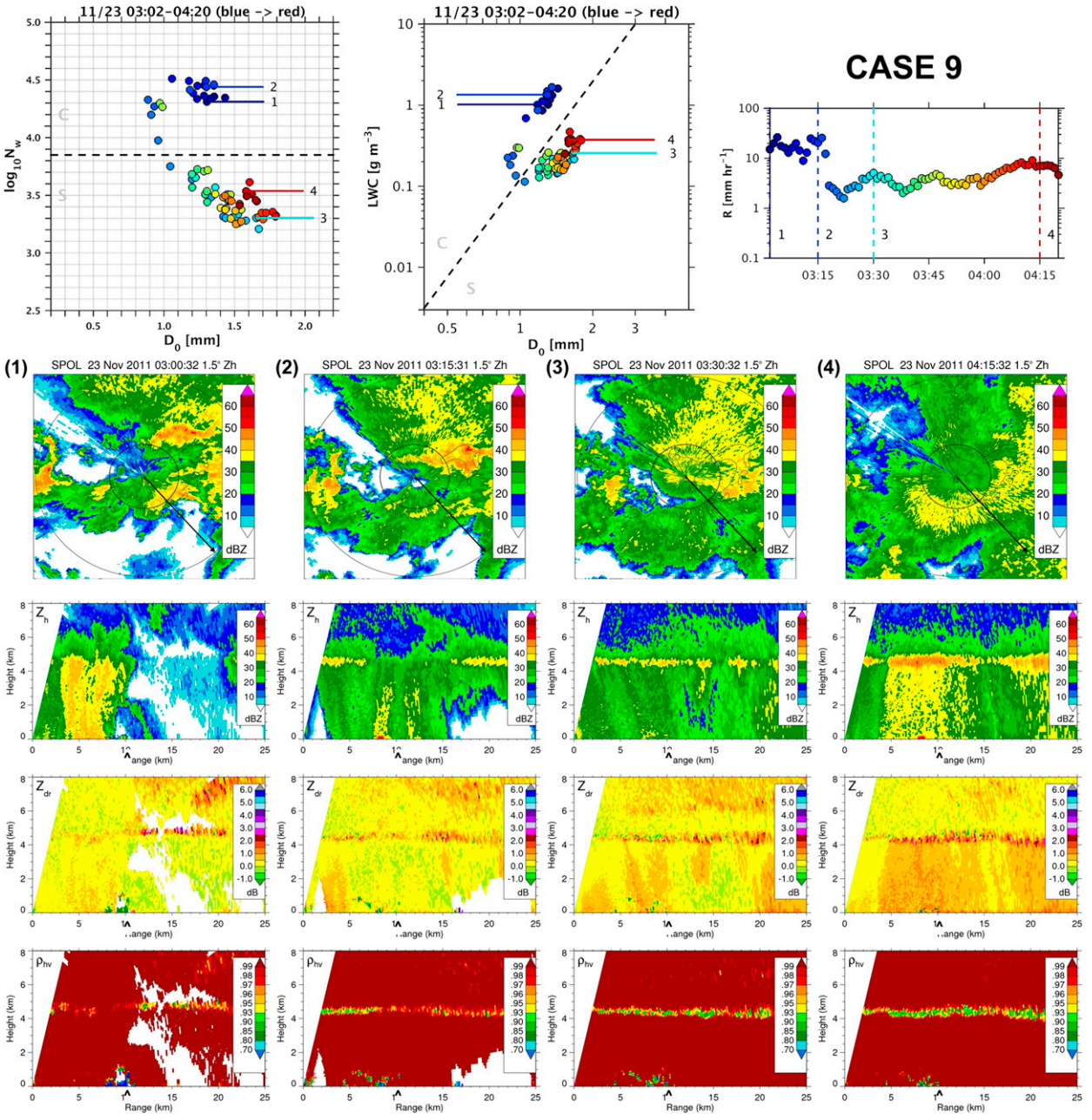

FIG. 13. Case study 9: as in Fig. 5, but for a transition from convection embedded in stratiform rain to strong stratiform rain at 0300, 0315, 0330, and 0415 UTC 23 Nov 2011 (corresponding to label numbers 1–4, respectively), with 2DVD data spanning 0302–0420 UTC. Numbers 1–4 correspond to callout points in the 2DVD data based on the time of the radar scans, where time increases as the colored markers go from blue to red.

illustrated in Fig. 13. The DSD and radar echoes begin in a similar fashion as the previous case, with only faint, disrupted signatures of melting in ρ_{hv} aloft and high $\log_{10}N_w$, LWC, and D_0 above each separation line. Rain rates reached 20 mm h^{-1} with surface Z_h just above 40 dBZ over the disdrometer. Radar echoes 15 min later in the second panel of the series look very similar to the decaying convection observed in the previous case study, with a fall streak of high reflectivity extending toward the ground and some lingering heterogeneity in the reflectivity pattern above discontinuous polarimetric signatures of melting near 5 km AGL. The DSD did not vary much between these two radar scans. Then, over the course of only five minutes, DSD shifted to the lower side of the $\log_{10}N_w^{\mathrm{SEP}}$ and LWC$^{\mathrm{SEP}}$ lines, and rain rates decreased to around 5 mm h^{-1}. The third set of RHIs just after the

transition show more horizontally homogeneous reflectivity patterns above the melting layer with increased Z_{dr}, Z_h, and reduced ρ_{hv} in the melting layer, suggesting more dominant stratiform rain processes throughout the column. The number concentration and LWC rapidly decreased as D_0 increased, consistent with the effects of snowflake aggregation aloft. The near-zero Z_{dr} layer above the bright band also supports this hypothesis.

This abrupt C/S transition was also reported as a number concentration jump by Waldvogel (1974), Tokay and Short (1996), and Braun and Houze (1994). According to the 372 case radar–2DVD case studies examined, while stratiform cases always exhibited lower $\log_{10}N_w$ than convection, the evolution between C/S rain was not usually as quick as this example. It is also interesting that D_0 and LWC vary in the same direction, or slope, as rain intensity varies within both stratiform and convective scenes, but the transition between the two rain types follows a different D_0 and LWC covariance not predicted by Eq. (1) (evidenced in both Figs. 12 and 13).

The DSD remained relatively constant in time until 45 min later in the fourth radar data example, when a strong radar bright band >50 dBZ developed above the disdrometer and led to $Z_{dr} > 1$ dB between 0 and 4 km AGL. The correlation ρ_{hv} was below 0.93, and Z_{dr} exceeded 3 dB over a relatively deep brightband depth compared to previous radar scans. Tokay et al. (1999) and Brandes et al. (2004) explained how surface D_0 often increases as brightband reflectivity and depth increase. Despite the intense stratiform bright band aloft, surface rain rates were still limited to about 9 mm h^{-1}.

j. Discussion

Convection was observed to rapidly evolve and decay, sometimes over very small spatial scales such that only a small portion of the convective radar echo actually went over the disdrometer. The resulting DSDs observed at the surface were therefore sometimes difficult to attribute to particular convective radar echoes because of the S-Pol's 15-min update time. DSDs in the intermediate time periods between convective updrafts or before and after their passage over the disdrometer were usually quite scattered. Likely because of drop size sorting in the turbulent cloud edge, the first and last few minutes of a convective DSD event sometimes exhibited very low number concentrations but very high D_0. For these reasons, Gunn and Marshall (1955) recount that rain usually begins with a few large drops, with moderate Z_h but only small rain rates. Despite these understandable fluctuations associated with convection, the cases with clear convective precipitation over the disdrometer were uniformly above the $\log_{10}N_w^{SEP} = 3.85$ line in the $N_w(D_0)$ parameter space. Stratiform rain DSD were more stable and slowly evolving. These stratiform radar echoes did not produce DSD above $\log_{10}N_w^{SEP} = 3.85$. Thus, we are most confident in our classification of stratiform DSD, while everything else warranted a convective classification. Given the consistency of radar observations in Figs. 5–13 of convection above, stratiform below, and transitions crossing the $\log_{10}N_w^{SEP} = 3.85$ line, maritime, tropical DSD data can apparently be separated by this method.

Yuter and Houze (2002) make an important point that, even if DSD separation methods can delineate C/S populations (as we demonstrate for this rain regime), a huge hurdle still remains if radar algorithms cannot. Radar observations in this section suggest that reflectivity texture-based algorithms and dual-polarization radar-based melting layer detection algorithms should be able to distinguish most types of tropical, oceanic rain consistently with this DSD-based approach. TH10 demonstrate this clearly for stratiform rain and strong convection using the BR09 DSD and Steiner et al. (1995) radar-based methods. However, light convective rain in Fig. 7 would be difficult to classify as convection using traditional radar-based techniques because of weak horizontal reflectivity gradients, overall low Z_h, and low echo-top heights. Another challenge for radar C/S algorithms is to detect convection embedded within stratiform rain (e.g., Fig. 12), especially if the convective echoes are shallow and exist below the radar bright band. Observations in this section showed that fall streaks within stratiform rain, associated with a relatively high surface rain rate up to 10 mm h^{-1} and Z_h up to 40 dBZ, were often the result of recently decayed convective activity (Yuter and Houze 1997, 1998). In Figs. 12 and 13, the DSDs settled down to the stratiform $N_w(D_0)$ and LWC(D_0) mode after the fall streak ended and once the reflectivity was more horizontally homogeneous above the bright band, as suggested by the Williams et al. (1995) vertically pointing radar classification method.

5. DSD-based convective/stratiform rain classification

In addition to analyzing 2DVD–radar case studies, we also explore a mathematical way to test which line, between $\log_{10}N_w^{SEP} = 3.7$ and 3.9, would minimize the most error in convective, stratiform, and total rainfall estimates. Since the S-Pol radar's scanning strategy prevented a paired 2DVD–radar comparison or statistical rainfall estimation analysis (see section 2), the same DSD-simulated reflectivity dataset used to form the $R(z)$ equations is used in a self-consistency test to see when the 2DVD total, convective, and stratiform

TABLE 3. Sensitivity of rain statistics to $\log_{10}N_w$ partitioning methods by comparing to Manus and Gan Island convective and stratiform 2DVD rain fractions and the percent difference between all, convective, and stratiform rain accumulations according to the 2DVD vs $R(z)_C$ and $R(z)_S$ calculations. These tests were run for convective/stratiform rain partitioning methods ranging from $\log_{10}N_w^{SEP} = 3.7$ to 3.9, where convection was classified above the line and stratiform at or below the separation line.

		2DVD				% diff 2DVD − C/S $R(z)$		
Place	$\log_{10}N_w^{SEP}$	Convective rain fraction (%)	Stratiform rain fraction (%)	Convective rain frequency (%)	Stratiform rain frequency (%)	R_{Total} (mm)	R_C (mm)	R_S (mm)
Manus	3.70	85	15	48	52	3.56	4.12	0.38
Gan		84	16	48	52	6.30	6.94	2.93
Manus	3.75	84	16	46	54	3.52	4.16	0.22
Gan		82	18	45	55	6.44	7.13	3.27
Manus	3.80	82	17	43	57	3.37	4.05	0.21
Gan		81	19	43	57	6.60	7.38	3.32
Manus	3.85	81	19	41	59	3.40	4.17	−0.01
Gan		80	20	41	59	6.55	7.41	3.22
Manus	3.90	79	21	38	62	3.46	4.43	−0.28
Gan		78	21	39	61	6.68	7.59	3.40

accumulated rainfall converged with $R(z)_C$ and $R(z)_S$ estimates. C/S $R(z)$ equations were iteratively formed with C/S R and z data as the partitioning line varied. The errors between the Gan 2DVD R and C/S $R(z)$ did not minimize for any particular separation line. However, this goal was achieved between $\log_{10}N_w^{SEP} = 3.8$ and 3.85 for Manus Island R, as seen in Table 3. The $\log_{10}N_w^{SEP} = 3.85$ dividing line was chosen between these two options in light of the consistent radar–2DVD case study observations of stratiform rain below this line in the previous section.

Table 3 also shows the variability in C/S rain fraction and frequency of occurrence estimates as the separation line varied. Moving the line from $\log_{10}N_w = 3.9$ to 3.7 accounted for a 6% decrease (increase) in convective (stratiform) rain fraction and a 10% decrease (increase) in convective (stratiform) rain frequency of occurrence at both locations. The case studies motivated $\log_{10}N_w^{SEP}$ somewhere between 3.8 and 3.9, so we consider a ± 0.05 $\log_{10}N_w$ window of uncertainty in rainfall estimates as a result of this separation technique. This window corresponds to 3% (2%) of total rainfall accumulation and 5% (4%) of rain occurrences.

The resulting Manus Island $R(z)_C$ and $R(z)_S$ equations according to the $\log_{10}N_w^{SEP} = 3.85$ separation appear in Table 4, along with equations from previous tropical, oceanic studies. The exponents and prefactors of the equations in Table 4 are consistent with the microphysical differences between C/S rain in equatorial, maritime regions documented in the previous section (Steiner et al. 2004). Statistics of D_0, D_{MAX}, $\log_{10}N_w$, and LWC for each C/S Manus Island population are shown in Table 5. By design, $\log_{10}N_w$ is higher for convection than stratiform rain. The D_0 and D_{MAX} 5%–95% ranges for each C/S population overlap substantially. However, there is a slight indication of higher D_0 in stratiform rain but higher D_{MAX} for convection, potentially because of the lack of vigorous riming processes in tropical, maritime convection. The LWC is understandably much greater in convection (95% value of 2.88 g m^{-3}) than stratiform (mostly below 0.33 g m^{-3}).

The C/S rain statistics using $\log_{10}N_w^{SEP} = 3.85$ are in Table 6. Stratiform (convective) rain at both locations makes up approximately 19% (81%) of the total rain accumulation but 59% (41%) of all rain occurrences. This high-resolution dataset indicates about a 10% higher convective rain fraction than previous maritime studies utilizing JWD disdrometers (Tokay and Short 1996) and radars (Steiner et al. 1995; Short et al. 1997; Atlas et al. 2000; TH10; Xu and Rutledge 2014), which

TABLE 4. The $R(z)$ equations from GATE (Hudlow 1979), TOGA COARE (Tokay and Short 1996), and MISMO (Yoneyama et al. 2008) field experiments, as well as new tropical, oceanic rain relationships derived from Manus and Gan Island 2DVD data (see domain in Fig. 1).

		GATE	TOGA COARE		MISMO	Gan and Manus Islands		
Equation	Parameter	All	C	S	All	All	C	S
$R = az^b$	a	0.013	0.032	0.011	0.027	0.021	0.037	0.026
	b	0.80	0.70	0.77	0.69	0.72	0.68	0.64
$Z = aR^b$	a	230	139	367	178	216	126	291
	b	1.25	1.43	1.30	1.44	1.39	1.46	1.55

TABLE 5. Mean, minimum, 5th percentile, 95th percentile, and maximum integral rain parameters for convective and stratiform DSD at Manus Island: max diameter D_{MAX} (mm); median diameter D_0 (mm); liquid water content LWC (g m^{-3}); number concentration $\log_{10}N_w$ (unitless).

Type	Parameter	Mean	Min	5%	95%	Max
C	D_{MAX}	2.17	0.80	0.95	3.91	7.65
S	D_{MAX}	2.15	0.80	1.04	3.51	8.54
C	D_0	1.04	0.34	0.56	1.59	2.29
S	D_0	1.16	0.48	0.68	1.69	3.83
C	LWC	0.71	0.01	0.03	2.88	12.64
S	LWC	0.10	0.00	0.01	0.33	4.53
C	$\log_{10}N_w$	4.25	3.85	3.89	4.68	5.22
S	$\log_{10}N_w$	3.33	1.57	2.81	3.79	3.85

are near 70/30 for C/S rain fraction and 30/70 for C/S frequency of occurrence. We hypothesize that previous radar-based methods were not able to adequately identify shallow, weak convection in this tropical, maritime rain regime because of the relatively lower resolution (~2 km) and the weak reflectivity gradients represented in interpolated, gridded radar datasets, low echo-top heights compared to C/S partitioning analysis level (usually performed at ~2–3 km), and overall lower Z_h associated with these oceanic echoes compared to land-based convection (Schumacher and Houze 2003). Section 2 explains why radar scanning geometry relative to the disdrometer prevented testing of this hypothesis in the current study.

Table 6 quantifies that, at both locations, about 30% of accumulated rainfall is due to rain with $R < 10\,\text{mm h}^{-1}$, which accounts for 87% of all rain occurrences. If a simple rule, such as classifying convection as any point with $R > 10\,\text{mm h}^{-1}$, were applied, the resulting, erroneous C/S rain fraction would be 87/13, and the erroneous C/S rain frequency fraction would be 71/29. Rain accumulation from this weak ($R < 10\,\text{mm h}^{-1}$) subset has equal volume contributions (14% of total rain volume each) from convective and stratiform DSD. If $R(z)_C$ and $R(z)_S$ are used on simulated reflectivity, and a single $R(z)_{ALL}$ equation is used to treat these convective DSD with $R < 10\,\text{mm h}^{-1}$ (14% of total rainfall at Manus Island), the estimated percentage of rainfall due to weak convection decreases to 11%. If a stratiform $R(z)_S$ is used in this context, in the case of a misclassification of weak, shallow convection as stratiform, the percentage of rain due to this population decreases further to 8%. If the lightly raining, convective DSD are treated with the appropriate $R(z)_C$ equation developed herein, their contribution to total rainfall is preserved. Similar results are found at Gan.

These statistics also show that almost two-thirds of the total raining occurrences come from stratiform rain $<10\,\text{mm h}^{-1}$ (58% of all rain), while one-third of occurrences originate from convection $<10\,\text{mm h}^{-1}$ (30% of all rain volume). The remaining 12% of occurrences

TABLE 6. Convective and stratiform rainfall accumulation and frequency of occurrence fractions according to Manus and Gan Island 2DVD rain rate R (mm h^{-1}) and $\log_{10}N_w^{SEP} = 3.85$ partitioning method.

Place	Rain type	% rain accumulation	% rain occurrence
Manus	Stratiform	19	59
Gan		20	59
Manus	Convective	81	41
Gan		80	41
Manus	$R < 10\,\text{mm h}^{-1}$	29	87
Gan		31	87
Manus	$R < 10\,\text{mm h}^{-1}$ that is	14	29
Gan	convective	16	30
Manus	$R < 10\,\text{mm h}^{-1}$ that is	14	—
Gan	convective using $R(z)_C$ on this weak convection	15	—
Manus	$R < 10\,\text{mm h}^{-1}$ that is	11	—
Gan	convective using $R(z)_{ALL}$ on this weak convection	12	—
Manus	$R < 10\,\text{mm h}^{-1}$ that is	8	—
Gan	convective using $R(z)_S$ on this weak convection	9	—
Manus	$R < 10\,\text{mm h}^{-1}$ that is	15	58
Gan	stratiform	15	58
Manus	% of convection with	18	70
Gan	$R < 10\,\text{mm h}^{-1}$	21	73
Manus	% of stratiform with	72	98
Gan	$R < 10\,\text{mm h}^{-1}$	75	98
Manus	% of convection with	33	82
Gan	$Z_h < 40$ dBZ	41	86
Manus	% of stratiform with	80	98
Gan	$Z_h < 40$ dBZ	73	97

are from convection with $R > 10\,\text{mm h}^{-1}$. Johnson et al. (1999) also found that shallow, trade wind cumulus clouds were much more abundant than cumulus congestus and deep convection during TOGA-COARE, even though more rain fell from the latter, more intense elements. According to the Manus and Gan Island datasets, only 18%–21% of the convective rain volume is from samples with $R < 10\,\text{mm h}^{-1}$, while 72%–75% of stratiform rain volume is due to these weak rain rates. Consistent with Johnson et al. (1999), 70% of all convective occurrences and 98% of all stratiform rain occurrences exhibited $R < 10\,\text{mm h}^{-1}$. Results are similar when C/S DSDs are thresholded by 40 dBZ.

Figure 14 illustrates the statistics from Table 6. The $N_w(D_0)$ and LWC(D_0) distributions have been colored by radar reflectivity and rain rate to show that a majority of both the convective and stratiform samples have rain rates less than $10\,\text{mm h}^{-1}$ and $Z_h < 40$ dBZ. For example, stratiform rain (below the new dashed separation lines) is mainly limited to below 40 dBZ and below $10\,\text{mm h}^{-1}$ near the surface, consistent with Tokay et al. (2001), Tokay and Short (1996), and others. It is interesting that the BR09 classification (solid separation line) is nearly

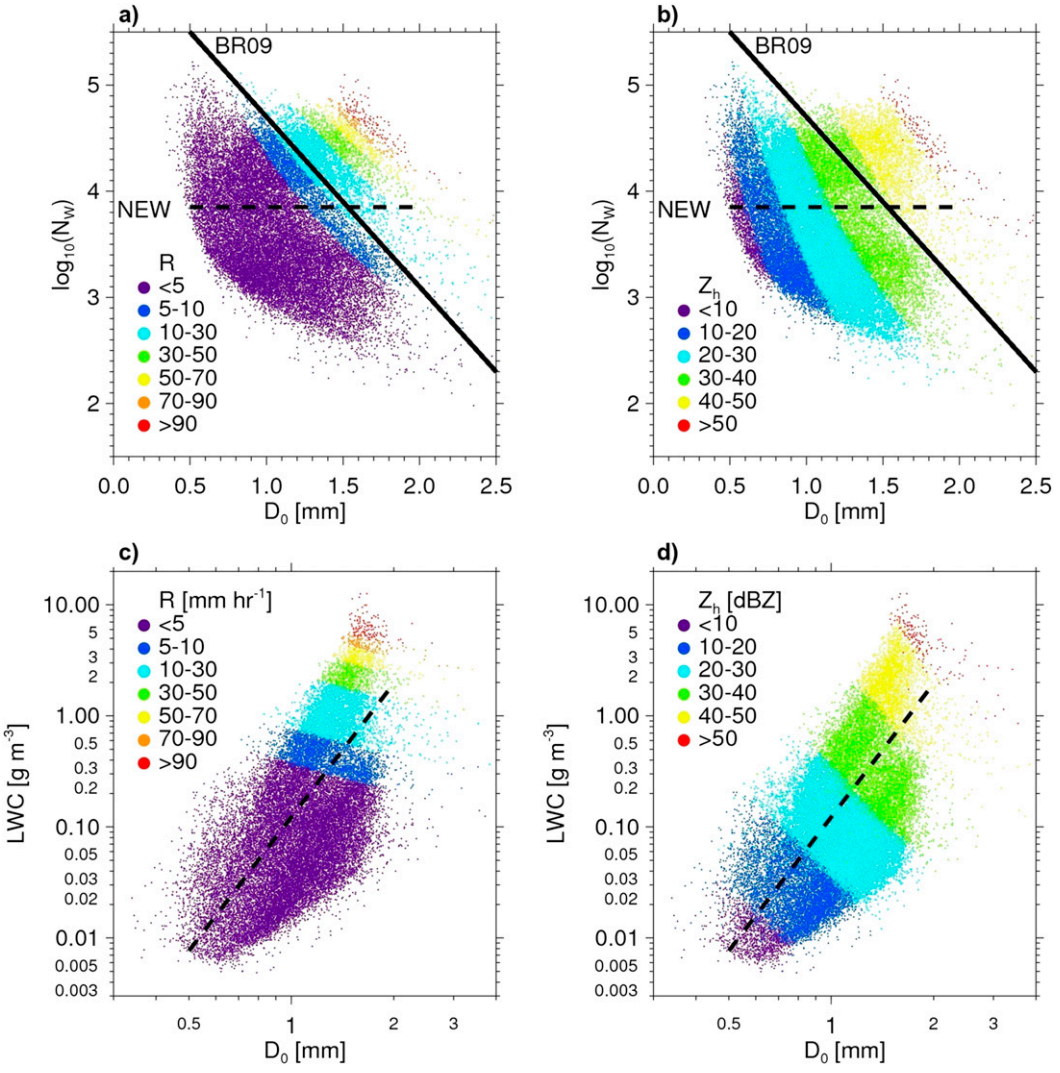

FIG. 14. Manus Island LWC(D_0) and $N_w(D_0)$ scatterplots color coded by 2DVD rain rate R and reflectivity Z_h, with the original subtropical, continental BR09 and updated tropical, oceanic C/S $\log_{10}N_w^{\mathrm{SEP}}$ separation lines. Similar distributions observed at Gan Island.

synonymous with a 40-dBZ or 10 mm h^{-1} threshold for these tropical, maritime datasets. While convection undoubtedly appears to exceed these thresholds and stratiform rain does not, the BR09 classification is too conservative for the weak, oceanic convection frequently observed at the Manus and Gan Islands as in Figs. 7, 8, and 9. Convection (above the new dashed separation lines) apparently manifests itself across the entire range of R and Z_h values (well below 10 mm h^{-1} and 40 dBZ), which was also shown by Bell and Suhasini (1994) and Zuidema et al. (2012). Thus, a major accomplishment of this study has been to modify the $N_w(D_0)$ BR09 C/S separation methodology to properly distinguish both strong and shallow weak maritime convection from stratiform rain in tropical, oceanic regions.

6. Implications for radar applications

a. C/S R(z) variability

Figure 14 also illustrates that convection has higher R and Z_h for a given D_0 than stratiform rain. The same D_0 can lead to a variety of reflectivities and rain rates depending on the number concentration. A physical interpretation is that higher N_w (during convection) for a given D_0 (which overlap between C/S rain) leads to greater LWC. The need to constrain $R(z)$ variability motivates radar classification of C/S echoes as well as formation and application of separate $R(z)$ equations for each rain type. Exploration of other integral rain parameter spaces further affirms that C/S modes of DSD variability exist within the Manus and Gan Island

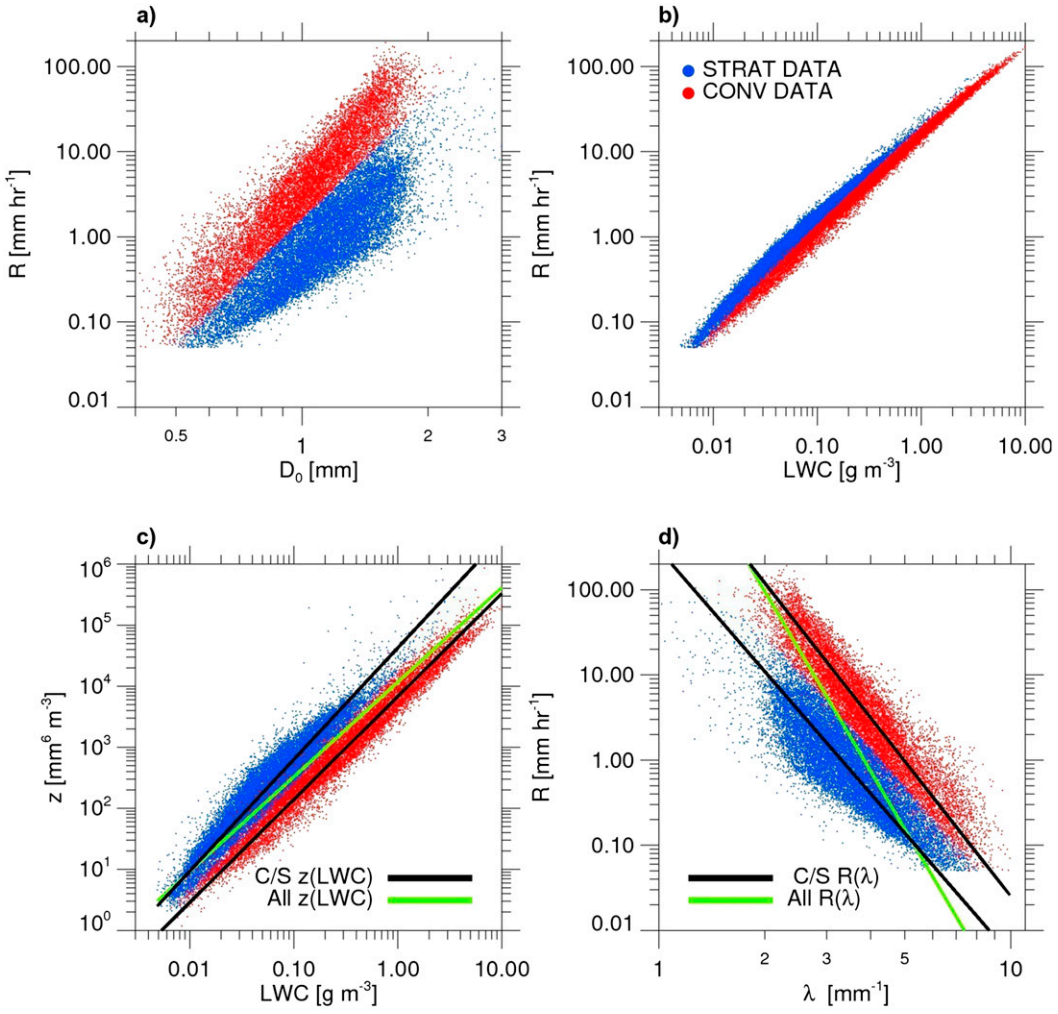

FIG. 15. Manus Island (a) $R(D_0)$, (b) R(LWC), (c) z(LWC), and (d) $R(\lambda)$ partitioned by the $\log_{10}N_w^{\mathrm{SEP}}$ line [stratiform (blue); convection (red)]. The z(LWC) and $R(\lambda)$ regression lines are superimposed in (c) and (d), respectively, for the entire DSD dataset (green) and each convective and stratiform population [black lines represent convective (stratiform) relationship on top (bottom) overlaying red (blue) points]. Similar distributions are observed at Gan Island.

datasets. Figure 15 shows that $R(D_0)$, R(LWC), z(LWC), and $R(\lambda)$ distributions consistently exhibit two populations that can be separated by $\log_{10}N_w^{\mathrm{SEP}}$ into S (blue) and C (red) modes. The separation between C/S rains in the $R(D_0)$ space is more distinct than that presented by Atlas et al. (2000). Convective rain achieves the same R as stratiform, but with lower D_0, higher log10N_w, and higher LWC. The overlapping z ranges between C and S rain reflect the fact that each of these DSD modes carry characteristically different LWC amounts for a given reflectivity (Table 5). The exponential DSD slope (λ) is flattened, or decreased, in stratiform precipitation associated with the aggregation of smaller crystals into larger snowflakes above the melting level (Lo and Passarelli 1982). Higher slope values are achieved during convection when new particles are formed via condensation, collision, and coalescence, also shown by Tokay and Short (1996). Orthogonal linear regression was used to relate z(LWC) and $R(\lambda)$ in C/S/all rain, which are presented in Table 7. The green all-data lines in Fig. 15 compromise a significant amount of DSD covariance described by each C/S best-fit line.

To investigate whether the aforementioned C/S DSD variability can account for any $R(z)$ variability during actual raining events, $R(z)$ distributions for all nine 2DVD–radar case studies are shown in Fig. 16. The $R(z)_{\mathrm{C}}$, $R(z)_{\mathrm{ALL}}$, and $R(z)_{\mathrm{S}}$ from Table 4 are shown for reference, with $R(z)_{\mathrm{C}}$ consistently yielding higher rain rates for a given Z_h than $R(z)_{\mathrm{S}}$. The $R(z)$ data from widespread, as well as isolated, strong convection (cases 1 and 2) were in

TABLE 7. Manus Island best-fit equations for rain rate R (mm h^{-1}) as a function of exponential DSD slope parameter λ (mm^{-1}) and radar reflectivity z (mm^6 m^{-3}) as a function of liquid water content LWC (g m^{-3}) for convective rain, stratiform rain, and all rain.

$$R_{ALL} = 12\,440.103\lambda^{-7.019}$$
$$R_C = 4617.2045\lambda^{-5.263}$$
$$R_S = 298.633\,45\lambda^{-4.766}$$
$$Z_{ALL} = 11\,668.466\mathrm{LWC}^{1.550}$$
$$Z_C = 6789.4854\mathrm{LWC}^{1.687}$$
$$Z_S = 42\,549.389\mathrm{LWC}^{1.829}$$

the high Z_h, high R spectrum aligned with $R(z)_C$ and therefore also $R(z)_{ALL}$, since they converge there. Case 3 exhibited shallow, weaker convection below 5 km and had lower Z_h with correspondingly lower R, most in line with $R(z)_C$ and well above $R(z)_{ALL}$. The isolated, weak convection below 4 km in case 4 had much lower R (<10 mm h^{-1}) but was aligned with $R(z)_C$ rather than $R(z)_S$. Even though warm rain processes in case 5 barely reached 3 km, the rain rates were slightly higher than in case 4 and also on the convective $R(z)_C$ line. In contrast, moderate stratiform rain rates at nearly the same intensity as the weakest, shallowest convective rain example hovered on the stratiform $R(z)_S$ line, just below 10 mm h^{-1}. Even lower rain rates in case 7 during weak stratiform rain were along $R(z)_S$ [in the region where $R(z)_{ALL}$ converges to $R(z)_S$]. Cases 8 and 9 showed transitions between embedded and leading convection, respectively, to heavy stratiform rain. Both cases showed migrations from $R(z)_C$, across $R(z)_{ALL}$, and to $R(z)_S$, with case 8's DSD after the fourth radar vertical cross section being more consistent with the weak stratiform rain from case 7.

Besides demonstrating consistency between the radar case study conclusions and the DSD partitioning method, another important result of these $R(z)$ case studies is that the $R(z)_{ALL}$ equation fit to the entire DSD dataset is hardly ever a "best fit" to individual cases of rain. The only exception is during the strongest convection or weakest stratiform rain, because $R(z)_{ALL}$ converges to either $R(z)_C$ or $R(z)_S$ at either endpoint. If an appropriate C/S partitioning method can be used, we believe this motivates formation and use of separate C/S $R(z)$ equations, because $R(z)_{ALL}$ lies between these two major modes of DSD variability (i.e., convective and stratiform rain).

Returning to the similarity observed between Manus and Gan Island DSD variability, Fig. 17 shows simulated radar reflectivity as a function of 2DVD rain rate for both locations. The $R(z)_{ALL}$ lines for each location are plotted together, illustrating that the similar distributions yield nearly identical $R(z)_{ALL}$ equations: $R(z)_{ALL} = 0.019z^{0.729}$ for Gan Island and $R(z)_{ALL} = 0.020z^{0.721}$ for Manus, which are equivalent to $z(R)_{ALL} = 228R^{1.37}$ at Gan and $z(R)_{ALL} = 216R^{1.39}$ at Manus. We move forward with the Manus Island equations (in Table 4), since they are based on 7 times as many points but appear to represent the same $R(z)$ variability observed at Gan Island. For instance, the second panel in Fig. 17 shows a histogram of the orthogonal distances between each (z, R) point and the Manus Island best-fit line. When normalized by the length of each dataset, the histograms are nearly equivalent. Both locations have the same percentage of $R(z)$ points scattered in each distance increment about the Manus Island best-fit line.

To examine these $R(z)$ distributions further, 2D histograms of $R(z)$ contoured by frequency of occurrence for both locations appear in Figs. 18a and 18b. A majority of the points lie below the $R(z)_{ALL}$ line for $Z_h < 30$–40 dBZ, with indication of another high density region of points above the line as $Z_h > 25$ dBZ. Figures 18c and 18d use Manus Island data and the $\log_{10}N_w^{SEP}$ method to confirm that the lower mode is classified as stratiform rain and the higher mode is classified as convective. Both these distributions are continuous, not disjointed, suggesting that the C/S partitioning algorithm was appropriate for this dataset. The $R(z)_{ALL}$ line lies between the convective and stratiform modes in a region of lower frequency of occurrence exhibiting moderate Z_h and R ranges.

Figure 19 more clearly demonstrates that C/S DSD variability in $\log_{10}N_w$ explains most of the $R(z)$ variability in these tropical, oceanic data. The $R(z)$ distribution is colored by median drop diameter and number concentration using the fuller Manus Island dataset (similar results found for Gan Island; not shown), akin to the rain parameter diagram of Ulbrich and Atlas (1978, 1998) and Steiner et al. (2004). Low $\log_{10}N_w$ ranges ≤3.85 only exist in the lower (stratiform) mode of the $R(z)$ distribution in Fig. 18. Likewise, high $\log_{10}N_w$ ranges >3.85 are only experienced in the upper (convective) $R(z)$ mode. Sauvageot and Lacaux (1995), Tokay et al. (1999), Testud et al. (2001), Morrison et al. (2009), TH10, and Bringi et al. (2012) also suggested that number concentration explained more rain variability over the tropical warm pool than variations in median drop diameter. This corresponds to concentration-controlled DSD variability, as opposed to size controlled or a combination thereof, described mathematically by Steiner et al. (2004). For instance, the two main $R(z)$ modes of variability in this dataset (Fig. 18) share nearly the entire range of median drop diameter D_0 but have mutually exclusive number concentration ($\log_{10}N_w$) ranges, which is consistent with Table 1, Table 5, and Figs. 3 and 4.

b. Radar-based C/S rainfall estimation

It is obvious from Figs. 16 and 18 how $R(z)_C$ and even $R(z)_{ALL}$ would overestimate stratiform rain if applied in

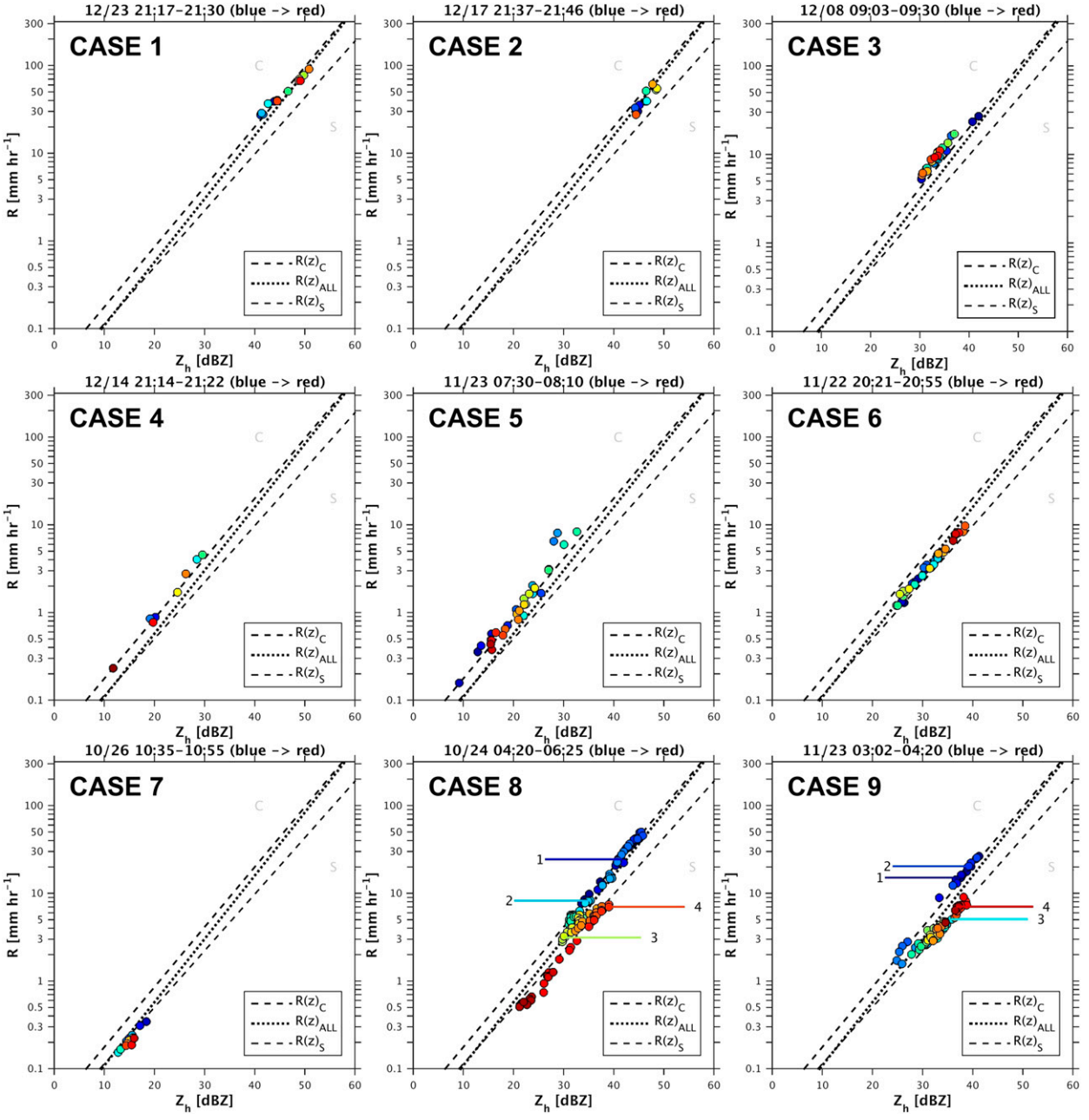

FIG. 16. The $R(z)$ for case studies 1–9, where time increases as the colored markers go from blue to red. Lines represent the $R(z)_C$ (upper), $R(z)_{ALL}$ (middle), and $R(z)_S$ (lower) best-fit equations shown.

the wrong context, and likewise how $R(z)_S$ and $R(z)_{ALL}$ would underestimate convective rain in many cases. Table 8 assesses the impacts of applying either a combination of $R(z)_C$ and $R(z)_S$ or $R(z)_{ALL}$ to the long-term simulated 2DVD radar reflectivity dataset. A 3% overestimation of total rain, 4% overestimation of convective rain, and only −0.01% underestimation of stratiform rain is encountered when using $R(z)_C$ and $R(z)_S$ for each distribution at Manus Is. compared to 2DVD R estimates. If the $R(z)_{ALL}$ equation is used only on the shallow, weak convective population, as in the case of uncertain C/S partitioning of this population, and separate $R(z)_C$ and $R(z)_S$ equations are used appropriately in all other instances, the total, convective, and stratiform rain accumulation errors are nearly zero. However, the percentage of rainfall by weak convection $<10\,\text{mm}\,\text{h}^{-1}$ is underestimated at 11% instead of 14% as indicated by the 2DVD (Table 6). If the $R(z)_S$

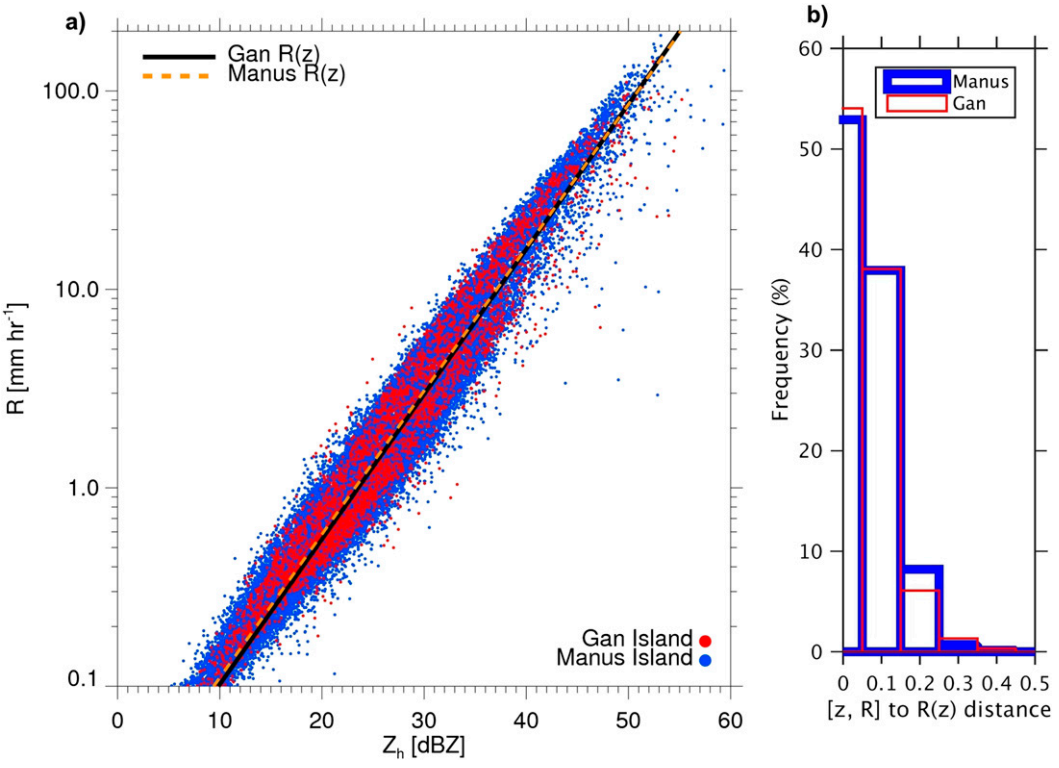

FIG. 17. (a) Gan and Manus Island 2DVD Z_h and R with linear regression best-fit lines for each location. (b) Normalized histograms of the orthogonal distance from each (z, R) point at each location to the Manus Island best-fit line. Distances are in logarithmic $R(z)$ units in both directions.

equation is used on weak, shallow convection, as in the case of a misclassification, the total rainfall is underestimated by 3%, convective rainfall amounts are underestimated by 4%, and stratiform rainfall is still well reproduced. The percentage of total rainfall due to weak, convection is further underestimated to 9% compared to 2DVD R or using $R(z)_C$ appropriately (Table 6). Using a simple $R > 10\,\mathrm{mm\,h^{-1}}$ threshold to denote convection and applying C/S $R(z)$ from this basis results in small total and convective rainfall errors, but a 17% overestimation of stratiform rainfall, which results in ±3% errors in S/C rain fraction. Therefore, using the individual C/S $R(z)$ relationships with inaccurate C/S partitioning method will produce misleading results. If radar-based C/S partitioning confidence is low, $R(z)_{ALL}$ should be used.

While the error in total rainfall accumulation is slightly lower (and negative) when using $R(z)_{ALL}$ compared to the C/S $R(z)$ method (−2.7%), this is overshadowed by vast over- and underestimations of stratiform (+59%) and convective (−15%) rain accumulation. Since $R(z)$ is a power-law equation, and the underestimation of high rain rates outweighs the underestimation of relatively lower rain rates, total rainfall is ultimately underestimated in this case. Similar to results by Testud et al. (2001), $R(z)_C$, $R(z)_S$, and $R(z)_{ALL}$ explain 98.5%, 96.4%, and 93.9% of the total variance in each respective population. Therefore, in addition to minimizing errors in C/S rain accumulation, using separate C/S $R(z)$ relations for each rain population can also help explain more total variance than a single $R(z)_{ALL}$.

The errors associated with using $R(z)_{ALL}$ have been quantified. For instance, even on these long-term Manus and Gan Island datasets, using the $R(z)_{ALL}$ equation on the entire dataset yields a ±10% difference in stratiform and convective rainfall fraction, respectively, compared to 2DVD R and C/S $R(z)$ estimates in Table 6. Differences in rainfall fraction estimates due to using $R(z)_{ALL}$ are expected to be higher for individual case studies when averaging over shorter time periods. Therefore, ±10% is considered to be the minimum error expected when estimating rainfall fraction caused by using $R(z)_{ALL}$ instead of distinguishing and treating C/S populations separately. Using $R(z)_C$ and $R(z)_S$ only produces a ±0.6% difference from 2DVD percentages of C/S rain fraction. When $R(z)_{ALL}$ or $R(z)_S$ are used for weak, shallow convection, and C/S $R(z)$

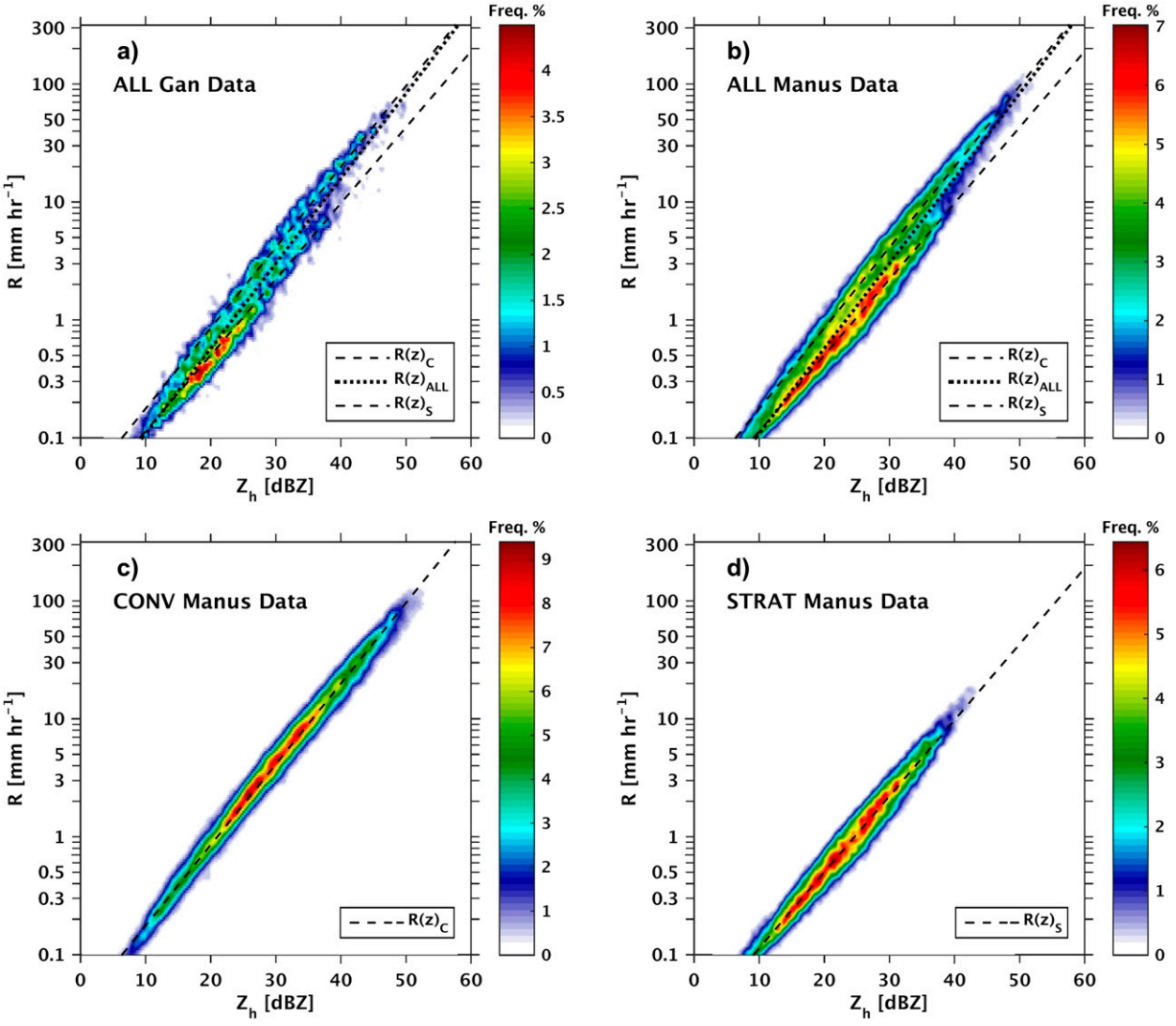

FIG. 18. Gan and Manus Island $R(z)$ smoothed 2D histograms contoured by frequency of occurrence with linear regression best-fit line from Manus Island. Gan Island: 180 bins in each direction and 6-bin Gaussian filter width. Manus Island number of bins in each direction: all = 280, convective = 200, stratiform = 235; 10-bin Gaussian filter width.

equations are used appropriately for the rest of the dataset, the C/S fractions of the resulting total rainfall from these methods hardly differ from 2DVD C/S fraction estimates and are of opposite sign than using C/S $R(z)$. However, Table 6 illustrates that the fraction of shallow, weak convective rain decreases from 14% to 11% using $R(z)_{\mathrm{ALL}}$ and to 8% using $R(z)_{\mathrm{S}}$ in this context.

We also consider the impact of using TOGA COARE and MISMO $R(z)$ relationships from Table 4 in Fig. 17 and Table 8, since these equations were formed with DSD in the equatorial west Pacific and Indian Oceans, respectively (Fig. 1). Although not plotted, the GATE and new $R(z)_{\mathrm{ALL}}$ equations are also very similar (Table 4). The TOGA COARE C/S relationships yield slightly different rainfall statistics than the new $R(z)_{\mathrm{C}}$ and $R(z)_{\mathrm{S}}$ relationships. Total rainfall and convective rainfall have similar errors as using the new C/S relationships, because the $R(z)_{\mathrm{C}}$ equations are nearly equivalent in Fig. 20 and Table 4. However, stratiform rain is strongly overestimated by the Tokay and Short (1996) $R(z)_{\mathrm{S}}$ compared to 2DVD R, because their $R(z)_{\mathrm{S}}$ has a lower slope. This leads to a $\pm$1.3 difference in S/C rainfall fraction compared to the 2DVD. Since Manus Island and TOGA-COARE are both in the western Pacific, this difference is most likely due to Tokay and Short's (1996) use of impact JWD disdrometers with less accurate small-drop

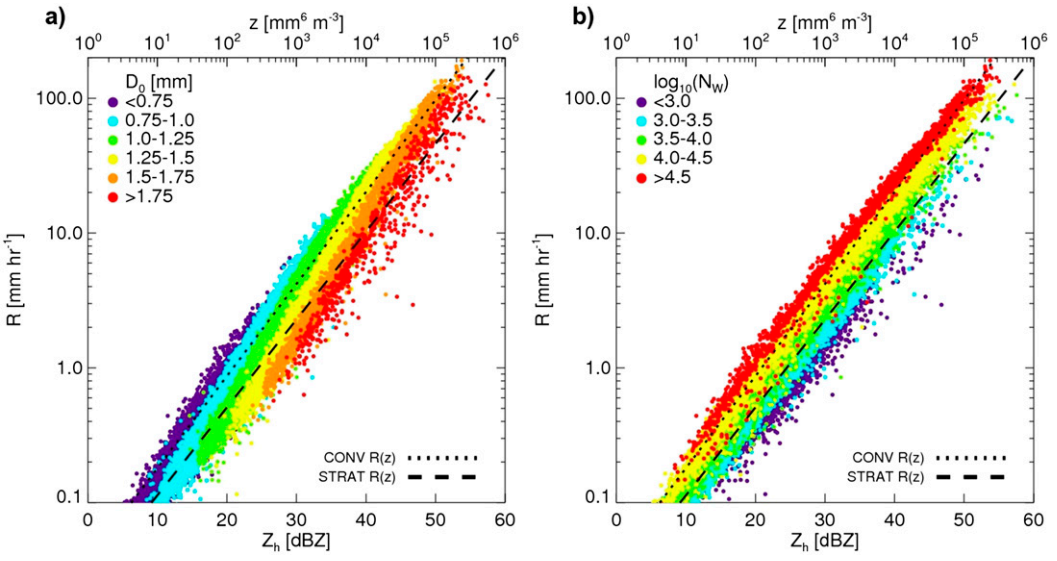

FIG. 19. Manus Island $R(z)$ color coded by (a) D_0 and (b) $\log_{10}N_w$ plotted with C/S $R(z)$.

detection, the nonnormalized[4] gamma DSD number concentration N_0, a probability matching method to find $R(z)$, different DSD data processing techniques, and/or resulting differences in C/S partitioning methods ($N_0^{\mathrm{SEP}} = 4 \times 10^9 R^{-4.9}$).

The MISMO relationship from JWD data is similar to $R(z)_{\mathrm{ALL}}$ in Fig. 20, except that it leans toward the convective DSD more than stratiform at the lower end of the $R(z)$ spectrum. This is because of this relationship's reliance on mostly convective DSD samples from only 6 weeks of data leading up to the active MJO, according to Yoneyama et al. (2008) and Masaki Katsumata (2006, personal communication). Thus, using the MISMO $R(z)_{\mathrm{ALL}}$ leads to an 11% overestimation (underestimation) of stratiform (convective) rain fraction compared to 2DVD R estimates (i.e., yielding a C/S rain fraction closer to 70/30). The errors on total, convective, and stratiform rainfall accumulation using the MISMO $R(z)$ compared to 2DVD estimates are relatively small for total rain accumulation, but are −13% for convective rain and +58% for stratiform rain.

Finally, we discuss the choice of $R(z)$ relationships relative to MJO evolution. DeWitt et al. (2013) described a central Indian Ocean evolution of aerosol loading as a function of MJO, which could impact the resultant DSDs. Similarly, Xu and Rutledge (2014) and Virts and Houze (2015) observed increased storm intensity and lightning activity leading up to the heaviest rain-producing phases of the MJO, which could also be related to DSD variability. However, it appears that the same $R(z)_{\mathrm{C}}$, $R(z)_{\mathrm{S}}$, and $R(z)_{\mathrm{ALL}}$ relationships are applicable during all phases of the MJO, because the LWC(D_0) and $N_w(D_0)$ covariance, as well as the $\log_{10}N_w^{\mathrm{SEP}} = 3.85$ separation between C and S rain are consistent regardless of rain intensity (Ulbrich and Atlas 1978). We make this distinction to emphasize that, while rain intensity and accumulation vary with MJO phase, the mean DSD variability over these open ocean locations, and therefore $R(z)$, should not be directly related to MJO phase. According to the long-term DSD datasets, it appears that only one version of the $R(z)_{\mathrm{S}}$, $R(z)_{\mathrm{C}}$, and $R(z)_{\mathrm{ALL}}$ equations is necessary for this tropical, oceanic rain regime. Furthermore, it would be inappropriate to partition $R(z)_{\mathrm{ALL}}$ by MJO phase because we have shown that the spread in $R(z)$ can be succinctly explained by mutually exclusive N_w differences between C and S rain, both of which are present during all phases of the MJO according to both Manus and Gan DSD datasets and other studies in these tropical ocean basins.

7. Conclusions

This study documented tropical, maritime DSD variability captured by the Gan and Manus Island 2DVDs with 3.5- and 18-month records in the equatorial Indian and west Pacific Oceans, respectively. The spectra of integral rain parameters and separation between convective (C) and stratiform (S) rain were similar at each

[4] We attempted to compute N_0 using μ estimated through our N_w and N_0 calculation method. However, μ varies greatly between raining clouds (BC01) and is not as well constrained by our data processing techniques as N_w and N_0. The resulting N_0 versus R distribution was very scattered. However, assuming $\mu = 0$ yielded rough agreement between our separation method and that presented by Tokay and Short (1996): $N_0^{\mathrm{SEP}} = 4 \times 10^9 R^{-4.9}$.

TABLE 8. Manus Island total, convective, and stratiform rainfall accumulation and C/S fraction of total rain. Estimates are from 2DVD rain rate R and various methods applied to 2DVD simulated z. Percent differences between 2DVD R and other R estimates are given. Percent differences between rain fractions are simply differences between fractions.

Place	R method	R_{Total} (mm)	R_{C} (mm)	R_{S} (mm)	% convective	% stratiform
Manus	2DVD	2627.33	2124.98	502.34	80.88	19.12
Gan		358.89	285.55	73.34	79.57	20.43
Manus	C/S $R(z)$	2716.65	2214.38	502.27	81.51	18.49
Gan		382.41	306.71	75.70	80.20	19.80
Manus	C/S $R(z)$ using $R(z)_{\text{ALL}}$ for weak C	2617.18	2114.90	502.27	80.81	19.19
Gan		372.45	293.09	79.37	78.69	21.31
Manus	C/S $R(z)$ using $R(z)_{\text{S}}$ for weak C	2542.54	2040.27	502.27	80.25	19.75
Gan		360.73	281.37	79.37	78.00	22.00
Manus	C/S $R(z)$ if C = $R > 10$ mm h^{-1}	2675.77	2086.47	589.30	77.98	22.02
Gan		386.88	297.68	89.19	76.95	23.05
Manus	$R(z)_{\text{ALL}}$	2555.85	1806.24	749.61	70.67	29.33
Gan		366.43	248.19	118.24	67.73	32.27
Manus	TOGA COARE C/S $R(z)$	2800.28	2227.22	573.06	79.54	20.46
Gan		402.98	309.95	93.03	76.91	23.09
Manus	MISMO $R(z)_{\text{ALL}}$	2628.39	1833.00	795.39	69.74	30.26
Gan		382.25	255.33	126.93	66.79	33.21
Manus	% diff: 2DVD – C/S $R(z)$	3.40	4.21	−0.01	0.63	−0.63
Gan		6.55	7.41	3.22	0.64	−0.64
Manus	% diff: 2DVD – C/S $R(z)$ using $R(z)_{\text{ALL}}$ for weak C	−0.39	−0.47	−0.01	−0.07	0.07
Gan		3.78	2.64	8.22	−0.87	0.87
Manus	% diff: 2DVD – C/S $R(z)$ using $R(z)_{\text{S}}$ for weak C	−3.23	−3.99	−0.01	−0.63	0.63
Gan		0.51	−1.47	8.22	−1.57	1.57
Manus	% diff: 2DVD – C/S $R(z)$ if C = $R > 10$ mm h^{-1}	1.84	−1.81	17.31	−2.90	2.90
Gan		7.80	4.25	21.62	−2.62	2.62
Manus	% diff: 2DVD – $R(z)_{\text{ALL}}$	−2.72	−15.00	49.22	−10.21	10.21
Gan		2.10	−13.08	61.22	−11.83	11.83
Manus	% diff: 2DVD – TOGA COARE C/S $R(z)$	6.58	4.81	14.08	−1.34	1.34
Gan		12.28	8.54	26.85	−2.65	2.65
Manus	% diff: 2DVD – MISMO $R(z)_{\text{ALL}}$	0.04	−13.74	58.34	−11.14	11.14
Gan		6.51	−10.59	73.08	−12.77	12.77

location, suggesting that cloud microphysical and dynamical properties are also similar at these locations. Both are open ocean locations with characteristically warm sea surface temperatures and influenced by similar large-scale forcing, such as the ITCZ and MJO. DSDs were characterized by high number concentrations (N_w) and small-to-medium drop diameters (95% of $D_0 <$ 1.7 mm; $D_{\text{MAX}} < 4$ mm) compared to continental DSDs. These DSDs were consistent with maritime, warm rain processes, such as condensation and coalescence, as well as some riming growth in more intense convection. In contrast, stratiform rain had an order of magnitude lower $\log_{10}N_w$ compared to convection, consistent with aggregation above the melting level.

The conceptual model in Fig. 21 illustrates the dominant cloud microphysical processes giving rise to Manus and Gan Island DSDs in various quadrants of the $N_w(D_0)$ space. Arrows indicate how intensifying stratiform and convective rain (i.e., higher reflectivity, higher rain rate, greater brightband intensity, or higher echo-top height) attain higher liquid water content and median raindrop diameters but maintain over an order of magnitude different N_w between C and S precipitation. Compared to weaker, shallower warm rain convection, stronger, deeper convection has higher D_0, consistent with deeper cloud depths. Stronger updrafts in these convective clouds promote higher liquid water contents, which also promote larger particle sizes.

The $\log_{10}N_w^{\text{SEP}} = 3.85$ line separating C and S rain was a modification of the BR09 partitioning method based on 372 paired dual-polarization radar–2DVD case studies and a quantitative C/S $R(z)$ self-consistency test. While a separation line may not appear physically satisfying at first, evaluation of radar echo and DSD evolution from all 372 case studies, previous observational studies, and theoretical evidence of number-controlled DSDs (Steiner et al. 2004) support our conclusion that number concentration is the most discerning feature between stratiform rain DSD and convective, maritime, tropical rain DSD. The new separation line is more applicable for tropical, oceanic rain regimes where weak convection ($R < 10$ mm h^{-1} and usually $Z_h < 35$ dBZ) is ubiquitous.

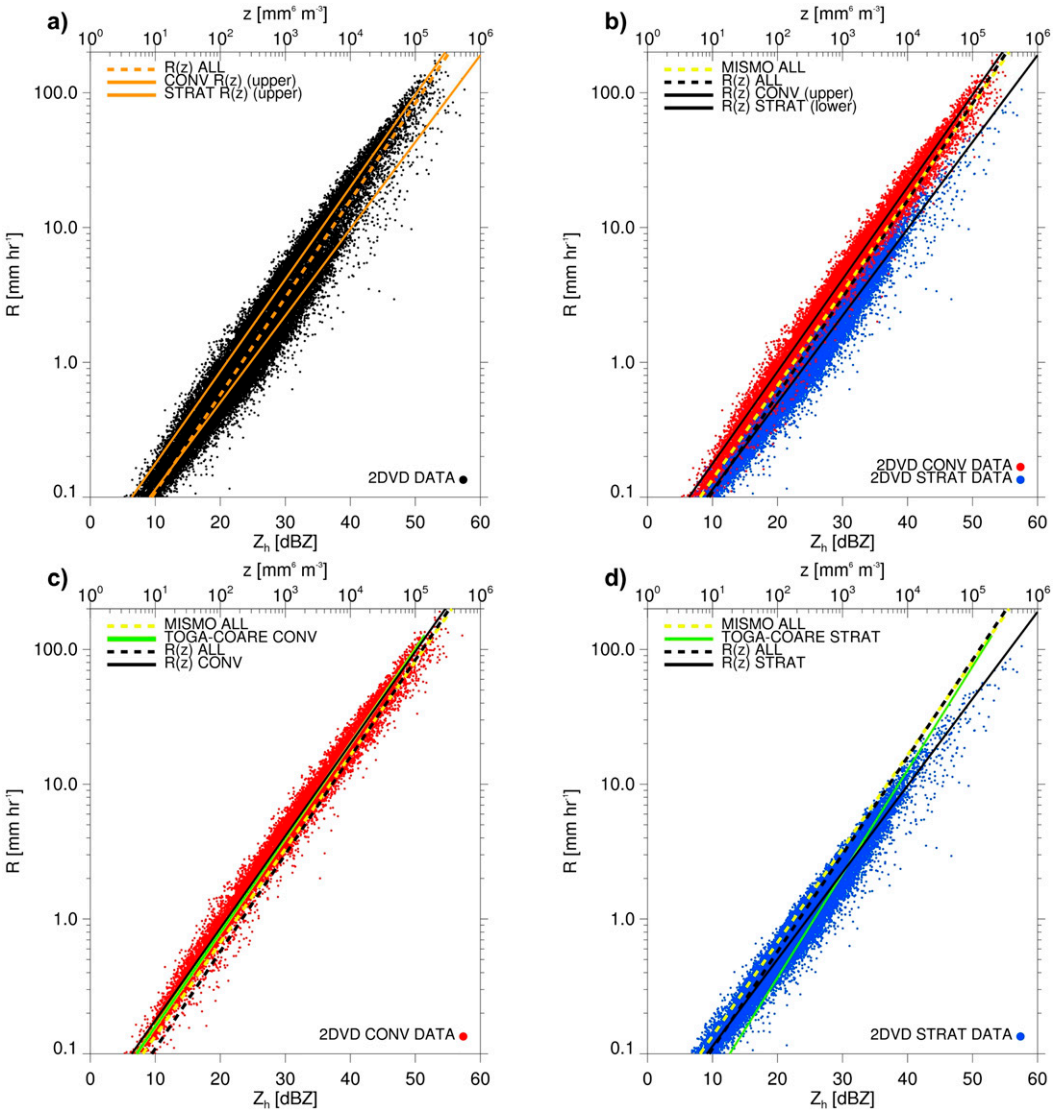

FIG. 20. Manus Island $R(z)$ scatterplots and regression lines for (a) the entire dataset, (b) the dataset partitioned into convective and stratiform populations according to the updated $\log_{10}N_w^{\mathrm{SEP}}$ method, (c) convective points, and (d) stratiform points. The $R(z)$ equations in Table 4 from MISMO, TOGA COARE, and the current study are plotted.

Weak, shallow convection by these metrics made up about 14% of rain volume and 30% of rain occurrences at the equatorial Indian and west Pacific sites. We offer evidence for increased convective rain fraction and frequency estimates compared to previous tropical, oceanic studies because our high-resolution DSD dataset and corresponding C/S partitioning algorithm provide better detection and treatment of this rain type. For instance, the DSD data yielded a long-term average 41/59 C/S rainfall frequency ratio and an 81/19 C/S rain fraction.

This long-term stratiform/convective rainfall fraction was found to vary by ±10%, respectively, when a single $R(z)_{\mathrm{ALL}}$ equation was used to calculate R compared to the directly sensed 2DVD R. In contrast, the 2DVD rain fraction estimate was recreated within ±0.6% when using $R(z)_{\mathrm{C}}$ and $R(z)_{\mathrm{S}}$ applied to the convective and stratiform rain populations, respectively. Use of separate C/S equations also minimized errors in convective and stratiform rain accumulation and statistically explained more R variance. Current radar-based C/S echo partitioning algorithms should be able to mimic the DSD-based classification technique with sufficient spatial and temporal resolution and tuning for the tropical, oceanic precipitation regime. However, current radar-based C/S partitioning has considerable uncertainty in shallow, weak convection and convective elements embedded in stratiform rain. The benefits of using C/S $R(z)$ equations will not be realized if the partitioning is incorrect. If a confident

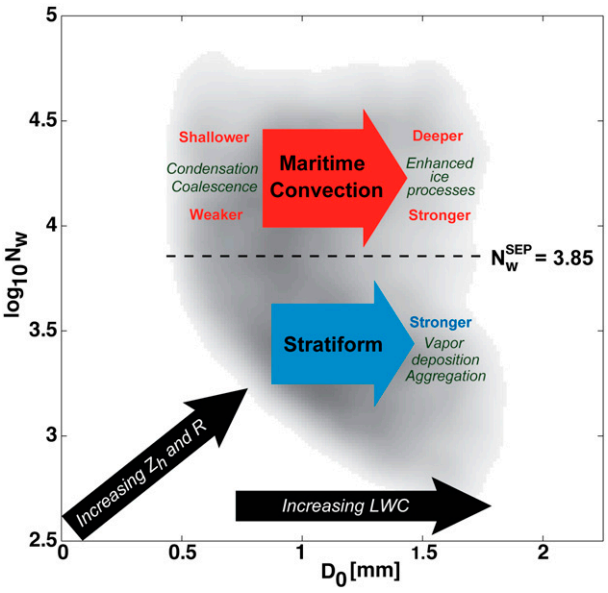

FIG. 21. Conceptual model of dominant microphysical processes (dark green) in the $N_w(D_0)$ space. The background is a grayscale smoothed contoured frequency 2D histogram showing darker (more frequent) DSD pairs from Manus Island 2DVD. Distinctions are made between maritime convection (red) and stratiform rain (blue) on either side of the updated $\log_{10}N_w^{SEP} = 3.85$ separator line. Thus, number concentration is the most distinguishing feature between stratiform and tropical, maritime convection. As rain intensity increases (i.e., larger rain rate R, radar reflectivity Z_h, bright band, or echo-top height), the median drop diameter D_0 and liquid water content LWC increase with much smaller variation in number concentration $\log_{10}N_w$ for either convective or stratiform rain. Thus, the red and blue arrows generally point in the direction of more intense convection and more intense stratiform precipitation by these metrics, respectively.

echo identification cannot be made, the best alternative is $R(z)_{ALL}$. A paired, statistical comparison between 2DVD and radar C/S classifications and rain rate would help quantify the uncertainty involved in application of different $R(z)$ relationships to real radar data but is not possible with the given datasets (explained in section 2).

This long-term, high-spatiotemporal-resolution dataset has provided new, comprehensive insights regarding tropical drop size distributions and rainfall variability since these types of data are not typically available in remote oceanic regions. Furthermore, characterizing and reducing the uncertainty associated with radar-based rainfall estimates is an important step toward confidently addressing more fundamental questions about tropical atmospheric dynamics and the contribution of freshwater into the oceans.

Acknowledgments. This research was funded by the NSF Graduate Research Fellowship Award DGE-1321845, NSF Award AGS-1063928, and DOE/ASR Award DE#SC0007016. We acknowledge DOE/ARM for supplying the long-term Manus and Gan Island 2DVD datasets. Thanks are given to Paul Hein and G. J. Huang for data management and processing (CSU). We appreciate conversations with Nick Guy (University of Wyoming), Robert Houze, Angela Rowe, and Scott Powell (University of Washington), Courtney Schumacher (TAMU), Scott Collis (Argonne National Laboratory), Christopher Williams (CIRES), as well as Elizabeth Barnes, Richard Johnson, John Peters, and Doug Stoltz (CSU). We are also particularly grateful to V. N. Bringi (CSU) for his insightful comments regarding this work. We also thank Michael Dixon, Bob Rilling, John Hubbert, and Scott Ellis (NCAR) for discussions concerning DYNAMO S-Pol radar data. We thank Chidong Zhang, Kunio Yoneyama, and Chuck Long for their leadership in the DYNAMO, CINDY, and AMIE projects, respectively. Three reviews helped improve the content and organization of this manuscript.

REFERENCES

Atlas, D., and C. W. Ulbrich, 2000: An observationally based conceptual model of warm oceanic convective rain in the tropics. *J. Appl. Meteor.*, **39**, 2165–2181, doi:10.1175/1520-0450(2001)040<2165:AOBCMO>2.0.CO;2.

——, R. C. Srivastava, and R. S. Sekhon, 1973: Doppler radar characteristics of precipitation at vertical incidence. *Rev. Geophys.*, **11**, 1–35, doi:10.1029/RG011i001p00001.

——, C. W. Ulbrich, and R. Meneghini, 1984: The multiparameter remote measurement of rainfall. *J. Hydrometeor.*, **19**, 3–22, doi:10.1029/RS019i001p00003.

——, ——, F. D. Marks Jr., E. Amitai, and C. R. Williams, 1999: Systematic variation of drop size and radar-rainfall relations. *J. Geophys. Res.*, **104**, 6155–6169, doi:10.1029/1998JD200098.

——, ——, ——, R. A. Black, E. Amitai, P. T. Willis, and C. E. Samsur, 2000: Partitioning tropical oceanic convective and stratiform rains by draft strength. *J. Geophys. Res.*, **105**, 2259–2267, doi:10.1029/1999JD901009.

Austin, P. M., and S. G. Geotis, 1979: Raindrop sizes and related parameters for GATE. *J. Appl. Meteor.*, **18**, 569–575, doi:10.1175/1520-0450(1979)018<0569:RSARPF>2.0.CO;2.

Barnes, H. C., and R. A. Houze Jr., 2013: The precipitating cloud population of the Madden–Julian oscillation over the Indian and west Pacific Oceans. *J. Geophys. Res. Atmos.*, **118**, 6996–7023, doi:10.1002/jgrd.50375.

——, and ——, 2014: Precipitation hydrometeor type relative to the mesoscale airflow in mature oceanic deep convection of the Madden–Julian oscillation. *J. Geophys. Res. Atmos.*, **119**, 13 990–14 014, doi:10.1002/2014JD022241.

——, M. D. Zuluaga, and R. A. Houze Jr., 2015: Latent heating characteristics of the MJO computed from TRMM observations. *J. Geophys. Res. Atmos.*, **120**, 1322–1334, doi:10.1002/2014JD022530.

Battan, L. J., 1973: *Radar Observation of the Atmosphere.* University of Chicago Press, 324 pp.

Bell, T. L., and R. Suhasini, 1994: Principal modes of variation of rain-rate probability distributions. *J. Appl. Meteor.*, **33**, 1067–1078, doi:10.1175/1520-0450(1994)033<1067:PMOVOR>2.0.CO;2.

Benedict, J. J., and D. A. Randall, 2007: Observed characteristics of the MJO relative to maximum rainfall. *J. Atmos. Sci.*, **64**, 2332–2354, doi:10.1175/JAS3968.1.

Biggerstaff, M. I., and R. A. Houze Jr., 1993: Kinematics and microphysics of the transition zone of the 10–11 June 1985 squall line. *J. Atmos. Sci.*, **50**, 3091–3110, doi:10.1175/1520-0469(1993)050<3091:KAMOTT>2.0.CO;2.

Brandes, E. A., and K. Ikeda, 2004: Freezing-level estimation with polarimetric radar. *J. Appl. Meteor.*, **43**, 1541–1553, doi:10.1175/JAM2155.1.

——, G. Zhang, and J. Vivekanandan, 2004: Drop size distribution retrieval with polarimetric radar: Model and application. *J. Appl. Meteor.*, **43**, 461–475, doi:10.1175/1520-0450(2004)043<0461:DSDRWP>2.0.CO;2.

Braun, S. A., and R. A. Houze Jr., 1994: The transition zone and secondary maximum of radar reflectivity behind a midlatitude squall line: Results retrieved from Doppler radar data. *J. Atmos. Sci.*, **51**, 2733–2755, doi:10.1175/1520-0469(1994)051<2733:TTZASM>2.0.CO;2.

Bringi, V. N., and V. Chandrasekar, 2001: *Polarimetric Doppler Weather Radar: Principles and Applications.* Cambridge University Press, 636 pp.

——, ——, J. Hubbert, E. Gorgucci, W. L. Randeu, and M. Schönhuber, 2003: Raindrop size distribution in different climatic regimes from disdrometer and dual-polarized radar analysis. *J. Atmos. Sci.*, **60**, 354–365, doi:10.1175/1520-0469(2003)060<0354:RSDIDC>2.0.CO;2.

——, C. R. Williams, M. Thurai, and P. T. May, 2009: Using dual-polarized radar and dual-frequency profiler for DSD characterization: A case study from Darwin, Australia. *J. Atmos. Oceanic Technol.*, **26**, 2107–2122, doi:10.1175/2009JTECHA1258.1.

——, M. A. Rico-Ramirez, and M. Thurai, 2011: Rainfall estimation with an operational polarimetric C-band radar in the United Kingdom: Comparison with a gauge network and error analysis. *J. Hydrometeor.*, **12**, 935–954, doi:10.1175/JHM-D-10-05013.1.

——, G.-J. Huang, S. J. Munchak, C. D. Kummerow, D. A. Marks, and D. B. Wolff, 2012: Comparison of drop size distribution parameter (D_0) and rain rate from S-band dual-polarized ground radar, TRMM precipitation radar (PR), and combined PR–TMI: Two events from Kwajalein Atoll. *J. Atmos. Oceanic Technol.*, **29**, 1603–1616, doi:10.1175/JTECH-D-11-00153.1.

Cheng, C. P., and R. A. Houze Jr., 1979: The distribution of convective and mesoscale precipitation in GATE radar echo patterns. *Mon. Wea. Rev.*, **107**, 1370–1381, doi:10.1175/1520-0493(1979)107<1370:TDOCAM>2.0.CO;2.

Cotton, W. R., G. H. Bryan, and S. C. van den Heever, 2011: *Storm and Cloud Dynamics.* International Geophysics Series, Vol. 99, Academic Press, 809 pp.

Cunning, J. B., and R. I. Sax, 1977: A Z–R relationship for the GATE B-scale array. *Mon. Wea. Rev.*, **105**, 1330–1336, doi:10.1175/1520-0493(1977)105<1330:ARFTGB>2.0.CO;2.

DeMott, C. A., and S. A. Rutledge, 1998a: The vertical structure of TOGA COARE convection. Part I: Radar echo distributions. *J. Atmos. Sci.*, **55**, 2730–2747, doi:10.1175/1520-0469(1998)055<2730:TVSOTC>2.0.CO;2.

——, and ——, 1998b: The vertical structure of TOGA COARE convection. Part II: Modulating influences and implications for diabatic heating. *J. Atmos. Sci.*, **55**, 2748–2762, doi:10.1175/1520-0469(1998)055<2748:TVSOTC>2.0.CO;2.

DeWitt, H. L., D. J. Coffman, K. J. Schulz, W. A. Brewer, T. S. Bates, and P. K. Quinn, 2013: Atmospheric aerosol properties over the equatorial Indian Ocean and the impact of the Madden–Julian oscillation. *J. Geophys. Res. Atmos.*, **94**, 1871–1891, doi:10.1002/jgrd.50419.

Funk, A., and C. Schumacher, 2013: Analysis of rain classifications over the tropics by version 7 of the TRMM PR 2A23 algorithm. *J. Meteor. Soc. Japan*, **91**, 257–272, doi:10.2151/jmsj.2013-302.

Gunn, K. L. S., and J. S. Marshall, 1955: The effect of wind shear on falling precipitation. *J. Meteor.*, **12**, 339–349, doi:10.1175/1520-0469(1955)012<0339:TEOWSO>2.0.CO;2.

Gunn, R., and G. D. Kinzer, 1949: The terminal velocity of fall for water droplets in stagnant air. *J. Meteor.*, **6**, 243–248, doi:10.1175/1520-0469(1949)006<0243:TTVOFF>2.0.CO;2.

Guy, N., and D. P. Jorgensen, 2014: Kinematic and precipitation characteristics of convective systems observed by airborne Doppler radar during the life cycle of a Madden–Julian oscillation in the Indian Ocean. *Mon. Wea. Rev.*, **142**, 1385–1402, doi:10.1175/MWR-D-13-00252.1.

Houze, R. A., Jr., 1997: Stratiform precipitation in regions of convection: A meteorological paradox? *Bull. Amer. Meteor. Soc.*, **78**, 2179–2196, doi:10.1175/1520-0477(1997)078<2179:SPIROC>2.0.CO;2.

——, 2004: Mesoscale convective systems. *Rev. Geophys.*, **42**, RG4003, doi:10.1029/2004RG000150.

Huang, G.-J., V. N. Bringi, and M. Thurai, 2008: Orientation angle distributions of drops after an 80-m fall using a 2D video disdrometer. *J. Atmos. Oceanic Technol.*, **25**, 1717–1723, doi:10.1175/2008JTECHA1075.1.

Hudlow, M. D., 1979: Mean rainfall patterns for the three phases of GATE. *J. Appl. Meteor.*, **18**, 1656–1669, doi:10.1175/1520-0450(1979)018<1656:MRPFTT>2.0.CO;2.

Illingworth, A. J., and T. M. Blackman, 2002: The need to represent raindrop size spectra as normalized gamma distributions for the interpretation of polarization radar observations. *J. Appl. Meteor.*, **41**, 286–297, doi:10.1175/1520-0450(2002)041<0286:TNTRRS>2.0.CO;2.

Islam, T., M. A. Rico-Ramirez, M. Thurai, and D. Han, 2012: Characteristics of raindrop spectra as normalized gamma distribution from a Joss–Waldvogel disdrometer. *Atmos. Res.*, **108**, 57–73, doi:10.1016/j.atmosres.2012.01.013.

Jakob, C., and C. Schumacher, 2008: Precipitation and latent heating characteristics of the major tropical western Pacific cloud regimes. *J. Climate*, **21**, 4348–4364, doi:10.1175/2008JCLI2122.1.

Johnson, R. H., and X. Lin, 1997: Episodic trade-wind regimes over the western Pacific warm pool. *J. Atmos. Sci.*, **54**, 2020–2034, doi:10.1175/1520-0469(1997)054<2020:ETWROT>2.0.CO;2.

——, and P. Ciesielski, 2013: Structure and properties of Madden–Julian oscillations deduced from DYNAMO sounding arrays. *J. Atmos. Sci.*, **70**, 3157–3179, doi:10.1175/JAS-D-13-065.1.

——, T. M. Rickenbach, S. A. Rutledge, P. E. Ciesielski, and W. H. Schubert, 1999: Trimodal characteristics of tropical convection. *J. Climate*, **12**, 2397–2418, doi:10.1175/1520-0442(1999)012<2397:TCOTC>2.0.CO;2.

Keenan, T. D., L. D. Carey, D. S. Zrnić, and P. T. May, 2001: Sensitivity of 5-cm wavelength polarimetric radar variables to raindrop axial ratio and drop size distribution. *J. Appl. Meteor.*, **40**, 526–545, doi:10.1175/1520-0450(2001)040<0526:SOCWPR>2.0.CO;2.

Kemball-Cook, S. R., and B. C. Weare, 2001: The onset of convection in the Madden–Julian oscillation. *J. Climate*, **14**, 780–793, doi:10.1175/1520-0442(2001)014<0780:TOOCIT>2.0.CO;2.

Kennedy, P. C., and S. A. Rutledge, 2011: S-band dual-polarization radar observations of winter storms. *J. Appl. Meteor. Climatol.*, **50**, 844–858, doi:10.1175/2010JAMC2558.1.

Kiladis, G. N., K. H. Straub, and P. T. Haertel, 2005: Zonal and vertical structure of the Madden–Julian oscillation. *J. Atmos. Sci.*, **62**, 2790–2809, doi:10.1175/JAS3520.1.

Kliche, D. V., P. L. Smith, and R. W. Johnson, 2008: L-moment estimators as applied to gamma drop size distributions. *J. Appl. Meteor. Climatol.*, **47**, 3117–3130, doi:10.1175/2008JAMC1936.1.

Kumjian, M. R., 2013: Principles and applications of dual-polarization weather radar. Part I: Description of the polarimetric radar variables. *J. Oper. Meteor.*, **1**, 226–242, doi:10.15191/nwajom.2013.0119.

——, and O. P. Prat, 2014: The impact of raindrop collisional processes on the polarimetric radar variables. *J. Atmos. Sci.*, **71**, 3052–3067, doi:10.1175/JAS-D-13-0357.1.

Lee, G. W., I. Zawadzki, W. Szyrmer, D. Sempere-Torres, and R. Uijlenhoet, 2004: A general approach to double-moment normalization of drop size distributions. *J. Appl. Meteor.*, **43**, 264–281, doi:10.1175/1520-0450(2004)043<0264:AGATDN>2.0.CO;2.

LeMone, M. A., E. J. Zipser, and S. B. Trier, 1998: The role of environmental shear and thermodynamic conditions in determining the structure and evolution of mesoscale convective systems during TOGA COARE. *J. Atmos. Sci.*, **55**, 3493–3518, doi:10.1175/1520-0469(1998)055<3493:TROESA>2.0.CO;2.

Lilly, D. K., 1960: On the theory of disturbances in a conditionally unstable atmosphere. *Mon. Wea. Rev.*, **88**, 1–17, doi:10.1175/1520-0493(1960)088<0001:OTTODI>2.0.CO;2.

Lin, X., and R. H. Johnson, 1996: Heating, moistening, and rainfall over the western Pacific warm pool during TOGA COARE. *J. Atmos. Sci.*, **53**, 3367–3383, doi:10.1175/1520-0469(1996)053<3367:HMAROT>2.0.CO;2.

Lo, K. K., and R. E. Passarelli, 1982: The growth of snow in winter storms: An airborne observational study. *J. Atmos. Sci.*, **39**, 697–706, doi:10.1175/1520-0469(1982)039<0697:TGOSIW>2.0.CO;2.

Mapes, B., S. Tulich, J. Lin, and P. Zuidema, 2006: The mesoscale convection life cycle: Building block or prototype for large-scale tropical waves? *Dyn. Atmos. Oceans*, **42**, 3–29, doi:10.1016/j.dynatmoce.2006.03.003.

Marshall, J. S., and W. M. K. Palmer, 1948: The distribution of raindrops with size. *J. Meteor.*, **5**, 165–166, doi:10.1175/1520-0469(1948)005<0165:TDORWS>2.0.CO;2.

Matsuno, T., 1966: Quasi-geostrophic motions in the equatorial area. *J. Meteor. Soc. Japan*, **44**, 25–53.

Minor, H. A., R. M. Rauber, S. Göke, and L. D. Girolamo, 2011: Trade wind cloud evolution observed by polarization radar: Relationship to giant condensation nuclei concentrations and cloud organization. *J. Atmos. Sci.*, **68**, 1075–1096, doi:10.1175/2010JAS3675.1.

Mishchenko, M. I., L. D. Travis, and D. W. Mackowski, 1996: T-matrix computations of light scattering by nonspherical particles: A review. *J. Quant. Spectrosc. Radiat. Transfer*, **55**, 535–575, doi:10.1016/0022-4073(96)00002-7.

Morrison, H., G. Thompson, and V. Tatarskii, 2009: Impact of cloud microphysics on the development of trailing stratiform precipitation in a simulated squall line: Comparison of one- and two-moment schemes. *Mon. Wea. Rev.*, **137**, 991–1007, doi:10.1175/2008MWR2556.1.

Munchak, S. J., C. D. Kummerow, and G. Elsaesser, 2012: Relationships between the raindrop size distribution and properties of the environment and clouds inferred from TRMM. *J. Climate*, **25**, 2963–2978, doi:10.1175/JCLI-D-11-00274.1.

Nitta, T., and S. Esbensen, 1974: Heat and moisture budget analyses using BOMEX data. *Mon. Wea. Rev.*, **102**, 17–28, doi:10.1175/1520-0493(1974)102<0017:HAMBAU>2.0.CO;2.

Penide, G., V. V. Kumar, A. Protat, and P. T. May, 2013: Statistics of drop size distribution parameters and rain rates for stratiform and convective precipitation during the north Australian wet season. *Mon. Wea. Rev.*, **141**, 3222–3237, doi:10.1175/MWR-D-12-00262.1.

Powell, S. W., and R. A. Houze Jr., 2013: The cloud population and onset of the Madden–Julian oscillation over the Indian Ocean during DYNAMO-AMIE. *J. Geophys. Res. Atmos.*, **118**, 11 979–11 995, doi:10.1002/2013JD020421.

Pruppacher, H. R., and J. D. Klett, 1997: *Microphysics of Clouds and Precipitation.* 2nd ed. Kluwer Academic Publishers, 954 pp.

Rauber, R. M., and Coauthors, 2007: Rain in shallow cumulus over the ocean: The RICO campaign. *Bull. Amer. Meteor. Soc.*, **88**, 1912–1928, doi:10.1175/BAMS-88-12-1912.

Rickenbach, T. M., and S. A. Rutledge, 1998: Convection in TOGA COARE: Horizontal scale, morphology, and rainfall production. *J. Atmos. Sci.*, **55**, 2715–2729, doi:10.1175/1520-0469(1998)055<2715:CITCHS>2.0.CO;2.

Riley, E. M., B. E. Mapes, and S. N. Tulich, 2011: Clouds associated with the Madden–Julian oscillation: A new perspective from CloudSat. *J. Atmos. Sci.*, **68**, 3032–3051, doi:10.1175/JAS-D-11-030.1.

Rowe, A. K., and R. A. Houze Jr., 2014: Microphysical characteristics of MJO convection over the Indian Ocean during DYNAMO. *J. Geophys. Res. Atmos.*, **119**, 2543–2554, doi:10.1002/2013JD020799.

Ruppert, J. H., and R. H. Johnson, 2015: Diurnally modulated cumulus moistening in the preonset stage of the Madden–Julian oscillation during DYNAMO. *J. Atmos. Sci.*, **72**, 1622–1647, doi:10.1175/JAS-D-14-0218.1.

Ryzhkov, A. V., S. E. Giangrande, V. M. Melnikov, and T. J. Schuur, 2005: Calibration issues of dual-polarization radar measurements. *J. Atmos. Oceanic Technol.*, **22**, 1138–1155, doi:10.1175/JTECH1772.1.

Salles, C., and J.-D. Creutin, 2003: Instrumental uncertainties in *Z–R* relationships and raindrop fall velocities. *J. Appl. Meteor.*, **42**, 279–290, doi:10.1175/1520-0450(2003)042<0279:IUIZRR>2.0.CO;2.

Sauvageot, H., and J.-P. Lacaux, 1995: The shape of averaged drop size distributions. *J. Atmos. Sci.*, **52**, 1070–1083, doi:10.1175/1520-0469(1995)052<1070:TSOADS>2.0.CO;2.

Schönhuber, M., G. Lammer, and W. L. Randeu, 2008: The 2D-Video-Disdrometer. *Precipitation: Advances in Measurement, Estimation and Prediction*. S. Michaelides, Ed. Springer, 3–31 pp., doi:10.1007/978-3-540-77655-0_1.

Schumacher, C., and R. A. Houze Jr., 2003: The TRMM precipitation radar's view of shallow, isolated rain. *J. Appl. Meteor.*, **42**, 1519–1524, doi:10.1175/1520-0450(2003)042<1519:TTPRVO>2.0.CO;2.

——, ——, and I. Kraucunas, 2004: The tropical dynamical response to latent heating estimates derived from the TRMM precipitation radar. *J. Atmos. Sci.*, **61**, 1341–1358, doi:10.1175/1520-0469(2004)061<1341:TTDRTL>2.0.CO;2.

——, S. N. Stevenson, and C. R. Williams, 2015: Vertical motions of the tropical convective cloud spectrum over Darwin, Australia. *Quart. J. Roy. Meteor. Soc.*, **141**, 2277–2288, doi:10.1002/qj.2520.

Seo, H., A. C. Subramanian, A. J. Miller, and N. R. Cavanaugh, 2014: Coupled impacts of the diurnal cycle of sea surface temperature on the Madden–Julian oscillation. *J. Climate*, **27**, 8422–8443, doi:10.1175/JCLI-D-14-00141.1.

Sharma, S., M. Konwar, D. K. Sarma, M. C. R. Kalapureddy, and A. R. Jain, 2009: Characteristics of rain integral parameters

during tropical convective, transition, and stratiform rain at Gadanki and its application in rain retrieval. *J. Appl. Meteor. Climatol.*, **48**, 1245–1266, doi:10.1175/2008JAMC1948.1.

Short, D. A., P. A. Kucera, B. S. Ferrier, J. C. Gerlach, S. A. Rutledge, and O. W. Thiele, 1997: Shipboard radar rainfall patterns within the TOGA COARE IFA. *Bull. Amer. Meteor. Soc.*, **78**, 2817–2836, doi:10.1175/1520-0477(1997)078<2817:SRRPWT>2.0.CO;2.

Smith, P. L., and D. V. Kliche, 2005: The bias in moment estimators for parameters of drop size distribution functions: Sampling from exponential distributions. *J. Appl. Meteor.*, **44**, 1195–1205, doi:10.1175/JAM2258.1.

Steiner, M., R. A. Houze Jr., and S. E. Yuter, 1995: Climatological characterization of three-dimensional storm structure from operational radar and rain gauge data. *J. Appl. Meteor.*, **34**, 1978–2007, doi:10.1175/1520-0450(1995)034<1978:CCOTDS>2.0.CO;2.

——, J. A. Smith, and R. Uijlenhoet, 2004: A microphysical interpretation of radar reflectivity–rain rate relationships. *J. Atmos. Sci.*, **61**, 1114–1131, doi:10.1175/1520-0469(2004)061<1114:AMIORR>2.0.CO;2.

Straka, J. M., D. S. Zrnić, and A. V. Ryzhkov, 2000: Bulk hydrometeor classification and quantification using polarimetric radar data: Synthesis of relations. *J. Appl. Meteor.*, **39**, 1341–1372, doi:10.1175/1520-0450(2000)039<1341:BHCAQU>2.0.CO;2.

Testud, J., S. Oury, R. A. Black, P. Amayenc, and X. Dou, 2001: The concept of ''normalized'' distribution to describe raindrop spectra: A tool for cloud physics and cloud remote sensing. *J. Appl. Meteor.*, **40**, 1118–1140, doi:10.1175/1520-0450(2001)040<1118:TCONDT>2.0.CO;2.

Thompson, E. J., S. A. Rutledge, B. Dolan, V. Chandrasekar, and B.-L. Cheong, 2014: A dual-polarization radar hydrometeor classification algorithm for winter precipitation. *J. Atmos. Oceanic Technol.*, **31**, 1457–1481, doi:10.1175/JTECH-D-13-00119.1.

Thurai, M., G. J. Huang, V. N. Bringi, W. L. Randeu, and M. Schönhuber, 2007: Drop shapes, model comparisons, and calculations of polarimetric radar parameters in rain. *J. Atmos. Oceanic Technol.*, **24**, 1019–1032, doi:10.1175/JTECH2051.1.

——, V. N. Bringi, and P. T. May, 2010: CPOL radar-derived drop size distribution statistics of stratiform and convective rain for two regimes in Darwin, Australia. *J. Atmos. Oceanic Technol.*, **27**, 932–942, doi:10.1175/2010JTECHA1349.1.

——, C. R. Williams, and V. N. Bringi, 2014: Examining the correlations between drop size distribution parameters using data from two side-by-side 2D-video disdrometers. *Atmos. Res.*, **144**, 95–110, doi:10.1016/j.atmosres.2014.01.002.

Tokay, A., and D. A. Short, 1996: Evidence from tropical raindrop spectra of the origin of rain from stratiform versus convective clouds. *J. Appl. Meteor.*, **35**, 355–371, doi:10.1175/1520-0450(1996)035<0355:EFTRSO>2.0.CO;2.

——, ——, C. R. Williams, W. L. Ecklund, and K. S. Gage, 1999: Tropical rainfall associated with convective and stratiform clouds: Intercomparison of disdrometer and profiler measurements. *J. Appl. Meteor.*, **38**, 302–320, doi:10.1175/1520-0450(1999)038<0302:TRAWCA>2.0.CO;2.

——, A. Kruger, and W. F. Krajewski, 2001: Comparison of drop size distribution measurements by impact and optical disdrometers. *J. Appl. Meteor.*, **40**, 2083–2097, doi:10.1175/1520-0450(2001)040<2083:CODSDM>2.0.CO;2.

——, P. G. Bashor, and K. R. Wolff, 2005: Error characteristics of rainfall measurements by collocated Joss–Waldvogel disdrometers. *J. Atmos. Oceanic Technol.*, **22**, 513–527, doi:10.1175/JTECH1734.1.

——, W. A. Petersen, P. Gatlin, and M. Wingo, 2013: Comparison of raindrop size distribution measurements by collocated disdrometers. *J. Atmos. Oceanic Technol.*, **30**, 1672–1690, doi:10.1175/JTECH-D-12-00163.1.

Twomey, S., 1977: The influence of pollution on the shortwave albedo of clouds. *J. Atmos. Sci.*, **34**, 1149–1152, doi:10.1175/1520-0469(1977)034<1149:TIOPOT>2.0.CO;2.

Uijlenhoet, R., M. Steiner, and J. A. Smith, 2003: Variability of raindrop size distributions in a squall line and implications for radar rainfall estimation. *J. Hydrometeor.*, **4**, 43–61, doi:10.1175/1525-7541(2003)004<0043:VORSDI>2.0.CO;2.

Ulbrich, C. W., 1983: Natural variations in the analytical form of the raindrop size distribution. *J. Climate Appl. Meteor.*, **22**, 1764–1775, doi:10.1175/1520-0450(1983)022<1764:NVITAF>2.0.CO;2.

——, and D. Atlas, 1978: The rain parameter diagram: Methods and applications. *J. Geophys. Res.*, **83**, 1319–1325, doi:10.1029/JC083iC03p01319.

——, and ——, 1998: Rainfall microphysics and radar properties: Analysis methods for drop size spectra. *J. Appl. Meteor.*, **37**, 912–923, doi:10.1175/1520-0450(1998)037<0912:RMARPA>2.0.CO;2.

——, and ——, 2002: On the separation of tropical convective and stratiform rains. *J. Appl. Meteor.*, **41**, 188–195, doi:10.1175/1520-0450(2002)041<0188:OTSOTC>2.0.CO;2.

——, and ——, 2007: Microphysics of raindrop size spectra: Tropical continental and maritime storms. *J. Appl. Meteor. Climatol.*, **46**, 1777–1791, doi:10.1175/2007JAMC1649.1.

Virts, K. S., and R. A. Houze Jr., 2015: Variation of lightning and convective rain fraction in mesoscale convective systems of the MJO. *J. Atmos. Sci.*, **72**, 1932–1944, doi:10.1175/JAS-D-14-0201.1.

Waldvogel, A., 1974: The N_0 jump of raindrop spectra. *J. Atmos. Sci.*, **31**, 1067–1078, doi:10.1175/1520-0469(1974)031<1067:TJORS>2.0.CO;2.

Waterman, P. C., 1971: Symmetry, unitarity, and geometry in electromagnetic scattering. *Phys. Rev.*, **3D**, 825–839, doi:10.1103/PhysRevD.3.825.

Webster, P. J., and R. Lukas, 1992: TOGA COARE: The Coupled Ocean–Atmosphere Response Experiment. *Bull. Amer. Meteor. Soc.*, **73**, 1377–1416, doi:10.1175/1520-0477(1992)073<1377:TCTCOR>2.0.CO;2.

Williams, C. R., W. L. Ecklund, and K. S. Gage, 1995: Classification of precipitating clouds in the tropics using 915-MHz wind profilers. *J. Atmos. Oceanic Technol.*, **12**, 996–1012, doi:10.1175/1520-0426(1995)012<0996:COPCIT>2.0.CO;2.

Willis, P. T., 1984: Functional fits to some observed drop size distributions and parameterization of rain. *J. Atmos. Sci.*, **41**, 1648–1661, doi:10.1175/1520-0469(1984)041<1648:FFTSOD>2.0.CO;2.

Wilson, E. A., A. L. Gordon, and D. Kim, 2013: Observations of the Madden Julian Oscillation during Indian Ocean Dipole events. *J. Geophys. Res. Atmos.*, **118**, 2588–2599, doi:10.1002/jgrd.50241.

Xu, W., and S. A. Rutledge, 2014: Convective characteristics of the Madden–Julian oscillation over the central Indian Ocean observed by shipborne radar during DYNAMO. *J. Atmos. Sci.*, **71**, 2859–2877, doi:10.1175/JAS-D-13-0372.1.

——, and ——, 2015: Morphology, intensity, and rainfall production of MJO convection: Observations from DYNAMO shipborne radar and TRMM. *J. Atmos. Sci.*, **72**, 623–640, doi:10.1175/JAS-D-14-0130.1.

Yanai, M., S. Esbensen, and J.-H. Chu, 1973: Determination of bulk properties of tropical cloud clusters from large-scale heat

and moisture budgets. *J. Atmos. Sci.*, **30**, 611–627, doi:10.1175/1520-0469(1973)030<0611:DOBPOT>2.0.CO;2.

Yoneyama, K., and Coauthors, 2008: MISMO field experiment in the equatorial Indian Ocean. *Bull. Amer. Meteor. Soc.*, **89**, 1889–1903, doi:10.1175/2008BAMS2519.1.

——, C. Zhang, and C. N. Long, 2013: Tracking pulses of the Madden–Julian oscillation. *Bull. Amer. Meteor. Soc.*, **94**, 1871–1891, doi:10.1175/BAMS-D-12-00157.1.

Yuter, S. E., and R. A. Houze Jr., 1997: Measurements of raindrop size distributions over the Pacific warm pool and implications for *Z–R* relations. *J. Appl. Meteor.*, **36**, 847–867, doi:10.1175/1520-0450(1997)036<0847:MORSDO>2.0.CO;2.

——, and ——, 1998: The natural variability of precipitating clouds over the western Pacific warm pool. *Quart. J. Roy. Meteor. Soc.*, **124**, 53–99, doi:10.1002/qj.49712454504.

——, and ——, 2002: Comment on ''Partitioning tropical oceanic convective and stratiform rains by draft strength'' by David Atlas et al. *J. Geophys. Res.*, **107**, doi:10.1029/2000JD000205.

Zhang, C., and S. M. Hagos, 2009: Bi-modal structure and variability of large-scale diabatic heating in the tropics. *J. Atmos. Sci.*, **66**, 3621–3640, doi:10.1175/2009JAS3089.1.

Zhu, S., X. Guo, G. Lu, and L. Guo, 2015: Ice crystal habits and growth processes in stratiform clouds with embedded convection examined through aircraft observation in northern China. *J. Atmos. Sci.*, **72**, 2011–2032, doi:10.1175/JAS-D-14-0194.1.

Zipser, E. J., 2003: Some views on ''hot towers'' after 50 years of tropical field programs and two years of TRMM data. *Cloud Systems, Hurricanes, and the Tropical Rainfall Measuring Mission (TRMM), Meteor. Monogr.*, No. 29, Amer. Meteor. Soc., 49, doi:10.1175/0065-9401(2003)029<0049:CSVOHT>2.0.CO;2.

——, and M. A. LeMone, 1980: Cumulonimbus vertical velocity events in GATE. Part II: Synthesis and model core structure. *J. Atmos. Sci.*, **37**, 2458–2469, doi:10.1175/1520-0469(1980)037<2458:CVVEIG>2.0.CO;2.

Zuidema, P., and Coauthors, 2012: On trade wind cumulus cold pools. *J. Atmos. Sci.*, **69**, 258–280, doi:10.1175/JAS-D-11-0143.1.

Zuluaga, M. D., and R. A. Houze Jr., 2013: Evolution of the population of precipitating convective systems over the equatorial Indian Ocean in active phases of the Madden–Julian oscillation. *J. Atmos. Sci.*, **70**, 2713–2725, doi:10.1175/JAS-D-12-0311.1.